Supplementary Information (SI) for Journal of Materials Chemistry A.

Supporting Information

A Highly Moisture-stable Ferroelectric Ammonium Phosphate Salt showing Piezoelectric Energy Harvesting and Rotation Sensing Applications

Vikash Kushwaha,[a] Neetu Prajesh,[a] Animesh Gopal,[b] Supriya Sahoo,[a] Swati Deswal,[a] Antonysylvester Kirana,[a] Kadhiravan Shanmuganathan [b,*] Jan K. Zaręba,[c,*] and Ramamoorthy Boomishankar[a,*]

[a]Department of Chemistry and Centre for Energy Science, Indian Institute of Science Education and Research, Pune, Dr. Homi Bhabha Road, Pune-411008, India

Email: boomi@iiserpune.ac.in

[b]Polymer Science and Engineering Division and Academy of Scientific and Innovative Research, CSIR National Chemical Laboratory, Dr. Homi Bhabha Road, Pune-411008, India

Email: k.shanmuganathan@ncl.res.in

[c]Institute of Advanced Materials, Wrocław University of Science and Technology, 50-370 Wrocław, Poland

Email: jan.zareba@pwr.edu.pl

Table of Contents

Experimental Section:

General Remarks

The starting materials bis(4-nitrophenyl) phosphate [$C_{12}H_9N_2O_8P$] and diisopropylamine were purchased from the BLD Pharma and used as received. The silicone elastomer base (Sylgard 184A) and silicone elastomer curing agent (Sylgard 184B) were purchased from the trademark of the Dow chemical company and used as received. NMR spectra were recorded on a Bruker or Jeol 400 MHz spectrometer ^{1}H NMR: 400.13 MHz ^{13}C {^{1}H} NMR: 100.62 MHz,^{31}P {^{1}H} NMR: 161.97 MHz) at low temperature and room temperature using $SiMe_4$ (^{1}H, ^{13}C) and 85% H_3PO_4 (^{31}P) as standards. The thermogravimetric and differential thermal analyses were performed using a PerkinElmer STA-6000 analyser in a nitrogen atmosphere at a 2 °C/min heating rate. Melting point analysis was performed using a Buchi M-650 melting point apparatus. FT-IR spectra were taken on a thermos-scientific Nicolet 6700 spectrophotometer operating in ATR mode. The variable temperature powder X-ray diffraction data were measured in the 2θ range of 5° to 50° on a Bruker-D8 Advance X-ray diffractometer. CD spectra were measured on the thin film of **DIPA·BNPP** using a JASCO J815 spectrometer from 500 nm to 190 nm. Elemental analyses were performed on a Vario-EL cube elemental analyzer. The solid-state UV-visible spectra of **DIPA·BNPP** were measured in an optical glass cuvette at room temperature using a Shimadzu UV-3600 spectrophotometer with a visible region range of 200-800 nm. The optical band gap was calculated from absorption spectra using the procedure described in the literature.[1, 2]

Synthesis of Diisopropylamino bis(4-nitrophenyl) phosphate (DIPA·BNPP): To a stirred solution of bis(4-nitrophenyl) phosphate (171.0 mg, 0.5 mmol) in 2:1 methanol/water mixture (7.5 mL), diisopropylamine (70 µL, 0.5 mmol) was added at room temperature. The resultant solution was filtered after 1 hour through a thick pad of celite and kept for crystallization under a slow evaporation method. Yellow rod-like crystals of **DIPA·BNPP** were obtained after 48 hours. Yield: 0.2 g (90.9%). M.P. 448-454 K. ^{31}P NMR (162 MHz, CD3OD) δ -11.23).^{1}H NMR (400 MHz, $CDCl_3$, ppm) δ 3.76–3.78 (d, 3H), 5.98-6.01 (m, 1H), 9.84-9.87 (d, 1H), 10.73- 1077 (d, 2H). FT-IR data in KBr pellet (cm^{-1}): 3747.94, 2738.32, 2522.28, 2357.47, 1588, 1514.05, 1486.35, 345, 1274.46, 1223.21, 1156.74, 1093.03, 885.2, 857.59, 731.56, and 692.7 cm^{-1} Anal. Calcd Formula. For $C_{18}H_{24}N_3O_8P$: C 48.98; H 5.48; N 9.53. Found: C 49; H 5.43; N 9.52.

X-ray Single Crystal Diffraction Analysis: The single-crystal X-ray diffraction analyses of **DIPA·BNPP** at various temperatures were performed on a Bruker Smart Apex Duo diffractometer using Mo K_α radiation (λ = 0.71073Å). The crystal structure was refined by full-matrix least-square against F^2 using all data from SHELXL built in the Apex 3 package.[3] The crystallographic refinement data for **DIPA·BNPP RT** at 150 and 298 K are listed in Table S1. All the non-hydrogen atoms were refined anisotropically. Hydrogen atoms were constructed in a geometric position relative to their parent atoms. One of the nitrophenyl groups was disordered at 150 K, while the other nitrate group was disordered at both 150 and 298 K. The atom positions of the disordered segments were restrained over only two positions using similar distances and similar U-restraints (SAME) of SHELX. The DIAMOND-3.1 and Mercury software packages were used to extract the bond lengths, bond angles and structural illustrations**.**

Theoretical calculations: Theoretical calculations were performed to investigate the gas-phase structure and properties of the **DIPA·BNPP** molecule using Gaussian 09 software.[4] Geometry optimizations and frequency analyses were carried out employing density functional theory (DFT) with the B3LYP functional and the 6-31G(d,p) basis set for all atoms. Mulliken atomic charges and electrostatic potential (ESP) analyses were conducted to assess the charge distribution across the molecule. Structural visualizations and molecular isosurface representations were generated within the Gaussian environment. For dipole moment calculations, a layered ONIOM approach was employed, wherein the anionic component of the system was treated as the high layer (QM region), and the cationic component was modelled as the low layer (MM region).

Hirshfeld Surface Analysis: To gain insight into the non-covalent interaction driving the crystal structure of compound **DIPA·BNPP**, a Hirshfeld surface mapping was performed using Crystal Explorer 3.1 based on the single-crystal X-ray data. This analysis enabled visualization of the various intermolecular forces at play. These intermolecular forces utilised different colour palettes, and the normalized contact distance (d_{norm}), shape index and curvedness were mapped onto the Hirshfeld surface of compound **DIPA·BNPP**, providing a visual representation of the strength of intermolecular interactions such as red colour for strong, blue for medium and white for weak intermolecular forces. The dimensionless quantity (shape index) reflects the local curvature of the Hirsfeld surface, with values between 1.0 and -1.0 denoting the most convex and concave regions, respectively. For the minimal surface regions, these values were fixed to be 0. The other term, curvedness, denotes a measure of how much the shape can get curved from the Hirshfeld surface, which has a general useful range of -4.0 to 0.4, respectively. In continuation, the 2D fingerprint plot of **DIPA·BNPP** can be constructed by the distance of an atom nearest to the interior (d_i) and exterior (d_e) of the generated Hirshfeld surface. The different contours (blue and grey color) in the 2D fingerprint plot explain the various types of molecular interactions, specific and all the contact information, based on the Hirshfeld surface. The surface generation of the Hirshfeld images can be constructed with an iso-value of a weight function of 0.5 a.u.

X-ray Photoelectron Spectroscopy: X-ray Photoelectron Spectroscopy (XPS) experiments were performed using a monochromatic Al Kα X-ray source (E_{ex} = 1486.0 eV) with an EA15 hemispherical Electron Energy Analyser, manufactured by PREVAC (Poland). The spectral acquisition was carried out in normal emission geometry with a pass energy of 200 eV. The X-ray source was operated at a power of 240 W and in the presence of a continuous flood (electron) source (Energy = 10.0 V; $I_{emission}$ = 10.0 µA). The samples were drop-casted and dried on a Si wafer (Merck), and the binding energies (BE) of elements were calibrated with respect to Si 2p photoemission at 99.3 ev. XPS spectra were recorded at 304 K while maintaining the base pressure of the analyser chamber better than $1x10^{-9}$ mbar.

Second Harmonic Generation (SHG) Measurements: A femtosecond laser system was employed for the Kurtz-Perry powder tests.[5] In this system a Coherent Astrella Ti: Sapphire regenerative amplifier (RA) was employed for generating ultrashort pulses of light (800 nm, 75 fs) at a repetition rate of 1 kHz. These pulses were then feeded into a wavelength-tuneable Topaz Prime Vis-NIR optical parametric amplifier (OPA) which was set to 1400 nm wavelength. Laser fluence at samples was equal to 0.19 mJ/cm^2. Estimation of the relative SHG efficiency of **DIPA·BNPP** was performed using the Kurtz-Perry powder method. As an SHG reference, potassium dihydrogen phosphate (KDP) was used. **DIPA·BNPP** and KDP were ground and sieved through an Aldrich mini sieve set, yielding a 250−177 µm microcrystal size fraction. The sieved samples were then sealed and placed in the sample holder after being secured between microscope glass slides (creating tightly packed layers). No refractive-index matching oil was employed. The laser beam was directed onto samples at 45° and was unfocused in all cases. Signal-collecting optics, mounted to the glass optical fibre, were placed perpendicularly to the plane of the sample (backscattering geometry), which was placed on a horizontally aligned holder. Scattered pumping radiation was suppressed using a 750 nm short-pass dielectric filter (FESH0750, Thorlabs). The spectra of diffused SHG were recorded by an Ocean Optics Flame T spectrograph.

Ferroelectric, Piezoelectric, and Dielectric studies: The *P-E* hysteresis loop measurement was performed on the thin film of **DIPA·BNPP** using a Sawyer-Tower circuit at room temperature. The thin film was prepared using the drop-casting method; 20 mg of **DIPA·BNPP** was dissolved in 0.5 ml of methanol and dropped onto the ITO-coated glass. The yellow-coloured micrometer-sized crystallites of **DIPA·BNPP** were observed on the ITO substrate after one hour. The conductive Indium-gallium alloy was used on opposite sides of the thin film which were presented as the top and bottom of the electrodes. The ferroelectric measurements were performed on an aixACCT TF2000E model hysteresis loop analyser. The hysteresis loop was obtained using the double-wave method by employing the positive up and negative down (PUND) function of the instrument at 1.92 Hz frequency. Leakage currents were collected dynamically for various voltage steps during the hysteresis loop measurements.

The piezoelectric charge coefficient (d_{33}) of **DIPA·BNPP** was measured on a poled pellet sample (thickness of 0.62 mm, diameter of 5 mm, poling field of 18.5 kV/cm) along the using the quasistatic (Berlincourt) method. An APC International wide-range d_{33} tester, operating with a force-frequency of 110 Hz and an amplitude of 0.25 N, was employed. The electrical contacts were made with silver conductive paste.

Temperature and frequency-dependent dielectric permittivity and dielectric loss measurements were performed on **DIPA·BNPP** pressed powder pellets. The measurements were conducted using the Solartron Analytical 1260 model Impedance Analyzer combined with a Dielectric Interface model 1296A. The sample was placed in a Janis 129610A cryostat sample holder, and a Lakeshore 336 model temperature controller was used to control the temperature.

Piezo-response force microscopy: The piezo-response analysis was performed on a single crystal of **DIPA·BNPP** grown on an ITO-coated glass substrate and employed to examine the domain structure and switching dynamics of **DIPA·BNPP**. The PFM measurements were performed using the Asylum Research MFP-3D atomic force microscopy (AFM) system. Contact mode AFM experiments were carried out using RMN-12PT300B cantilever probes, which had a spring constant of 1.12 N m^{-1} and a tip diameter of less than 8 nm, to measure the piezoresponse of the crystal films. PFM data was obtained through vertical-PFM experiments, wherein an AC voltage was applied to the conductive AFM tip while the bottom electrode remained grounded. The PFM images were collected at a resonance frequency of 300 +/- 20 kHz, with an applied bias of 100 V. Additionally, PFM phase and amplitude contrast were recorded using dual AC resonance tracking (DART) mode PFM.

Formation of polymer composite film and PENG: The polymer composite film was prepared using the previously reported procedure. We used 650 mg of poly (dimethyl siloxane) (PDMS) and 65 mg of curing agent added to a petri dish. **DIPA·BNPP** was incorporated into the petri dish according to the desired weight percentage of the composite, and the mixture was thoroughly mixed. Next, the polymer composite was spread over a 2.5 X 2.5 cm^2 sheet, followed by degassing. The mixture was left to cure at room temperature for five days until completely dried. Copper electrodes were affixed to opposite surfaces of the film, after which the device assembly was finalized by establishing electrical connections at the electrode terminals and encasing the entire structure in Kapton tape to safeguard it against physical damage. The energy harvesting performance of the **DIPA·BNPP**-PDMS composite devices was evaluated using a custom-built impact measurement setup. Output voltages were recorded with a Tektronix DMM 7510 7 ½ digital multimeter operating at an input impedance of 1 MΩ.

Stress-Strain Analysis: An Intron 5943 universal testing machine was used to compare the stress-strain behaviour of pure PDMS and **DIPA·BNPP**-PDMS composite films on rectangular film strips with 2 mm thickness, 5mm width and 20 mm length (gauge length: 10 mm, grip length: 7.5 mm each side) at a strain rate of 5mm/min. The load cell used for testing had a capacity of 1 kN.

Fabrication of RPM sensor: The contact-type RPM sensor device was fabricated employing a hollow plastic cylindrical pipe of 40 mm diameter and 30 mm height. A BLDC motor was fixed at one side of the cylinder. A plastic belt with a striker handle has been integrated into the rotating shaft of the motor, which can come into contact with the piezoelectric nanogenerator (PENG) device. The PENG device for the sensor was prepared by spin coating the 10 wt% **DIPA·BNPP**-PDMS composite film with Ag paste in toluene, which acts as the electrodes. Two connections using Cu wires have been incorporated at the top and bottom electrodes after ensuring easy accessibility to the motor shaft. The Ag electrodes were further safeguarded with Kapton adhesive tape to prevent damage from the mechanical action of the motor handle. A plastic rod adjacent to the PENG sensor has been placed to enhance the impact force on the sensor. This can be achieved by allowing the striking handle to brush the rod before touching the sensor. The response voltage generated from the PENG sensor is channelled into an Arduino microcontroller (ECU controller) using the Cu wires. In the PENG sensor device, the electrical signals are generated in a constant time interval as the speed of the motor remains constant during the experiment. The microcontroller senses the time difference between the signals and calculates the RPM using the expressions given in the supporting discussion 2 section (vide supra). These calculations were programmed into the microcontroller using C^{++} language.

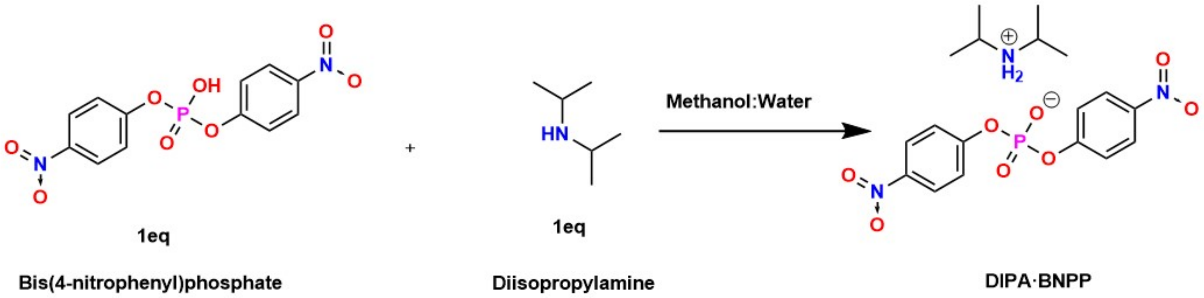

Figure S1. The schematic diagram for the synthesis of **DIPA·BNPP**.

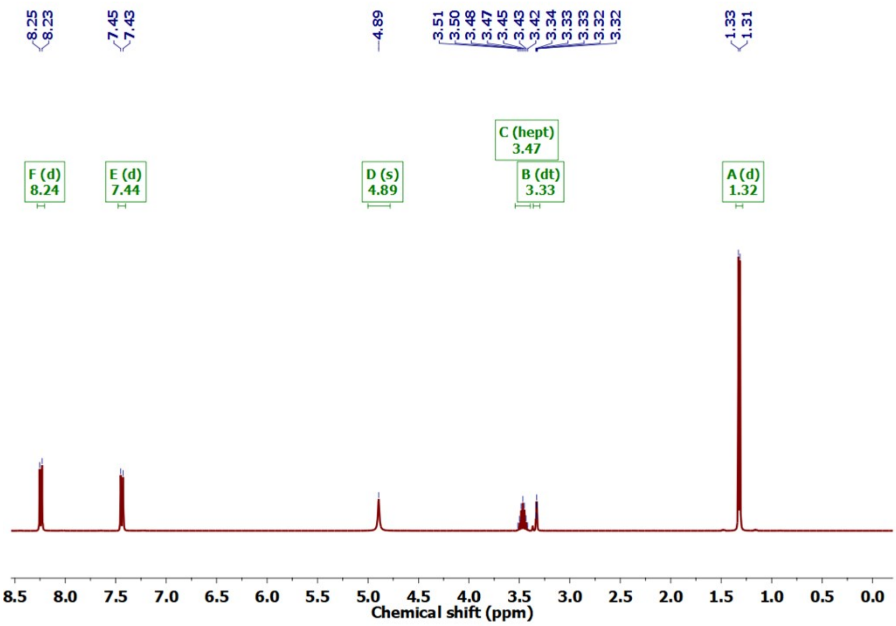

Figure S2. ^{1}H-NMR spectrum of **DIPA·BNPP** in methanol-d_4 at 298K.

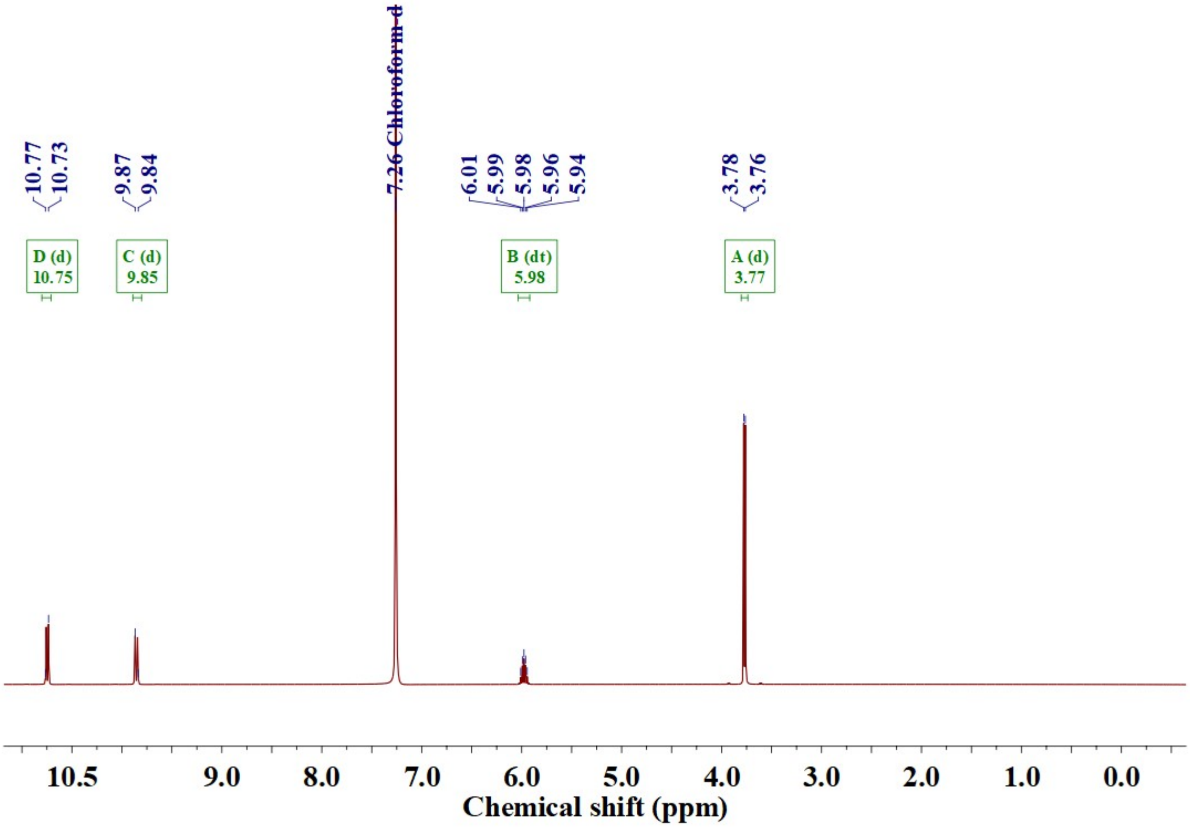

Figure S3. ^{1}H-NMR spectrum of **DIPA·BNPP** in $CDCl_3$ at 298K.

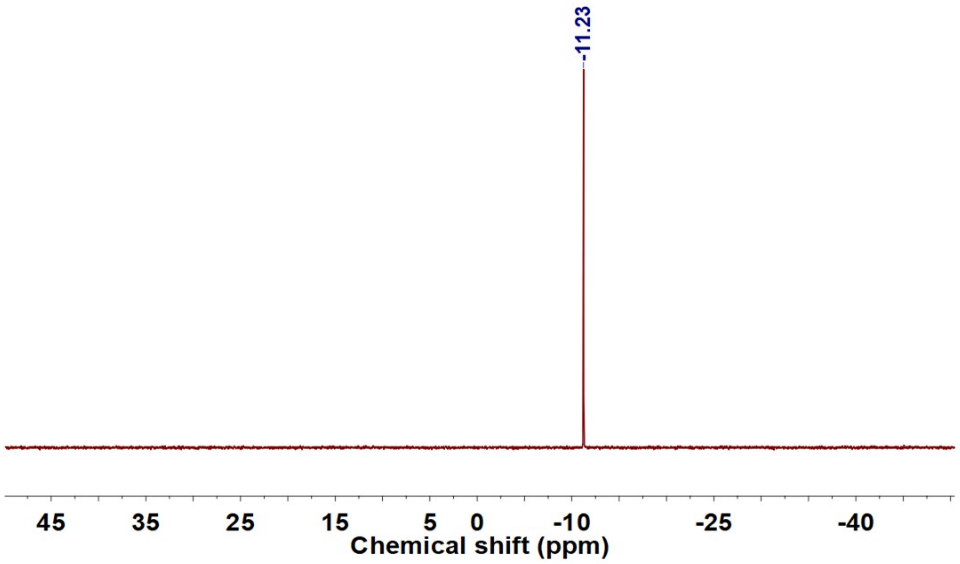

Figure S4. ^{31}P NMR of spectra of **DIPA·BNPP** in $CDCl_3$ at 298K.

Table S1. Crystallographic data and refinement statistics of **DIPA·BNPP** at different temperatures.

Crystal data	**DIPA·BNPP**	**DIPA·BNPP** RT
Chemical formula	$C_{18}H_{24}N_3O_8P$	$C_{18}H_{24}N_3O_8P$
Formula weight (g/mol)	441.37	441.37
Temperature (K)	150(2)	298(2)
Crystal system	Monoclinic	Monoclinic
Space group	*C*2	*C*2
a (Å); α (°)	a = 24.600(4) Å, α= 90°	a = 24.891(13) Å, α= 90°
b (Å); β (°)	b = 8.0170(15) Å, β= 101.633(5) °	b = 8.160(4) Å, β= 101.651(14) °
c (Å); ϒ (°)	c = 11.0146(19) Å, γ = 90°.	c = 11.052(6) Å, γ= 90°
V (Å^3); Z	2127.7(7), 4	2198.5(19), 4
ρ (calc.) g cm^{-3}	1.378	1.333
μ (Mo Kα) mm^{-1}	0.179	0.173
2θ$_{max}$ (°)	28.296°	28.468°
R(int)	0.0535	0.0994
Completeness to θ	100 %	99.9 %
Data / param.	5272 / 293	5489 / 283
GOF	1.015	1.015
R1 [I>2σ(I)]	0.0404	0.0558
wR2 (all data)	0.0.096	0.1603
Flack parameter	0.01(6)	-0.03(10)
max. peak/hole (e.Å^{-3})	0.292/ -0.298	0.318/-0.196

Table S2: Selected bond lengths [Å] and angles [°] of **DIPA·BNPP** at 150 and 298 K.

Compound	**Bond length (Å)**	**Bond angle (°)**
DIPA·BNPP (150 K)	P(1)-O(1) :1.474(2)	O(1)-P(1)-O(2): 122.49(11)
	P(1)-O(2) : 1.481(2)	O(1)-P(1)-O(4): 109.20(10)
	P(1)-O(4) : 1.6195(19)	O(2)-P(1)-O(4): 106.00(11)
	P(1)-O(3) : 1.623(2)	O(1)-P(1)-O(3): 105.50(11)
	O(3)-C(11): 1.388(6)	O(2)-P(1)-O(3): 109.41(11)
	O(3)-C(11') : 1.390(10)	O(4)-P(1)-O(3): 102.52(11)
	O(4)-C(21) : 1.395(3)	C(11)-O(3)-P(1): 123.1(9)
	N(1)-C(1) : 1.503(4)	C(11')-O(3)-P(1): 119.5(16)
	N(1)-C(4) : 1.504(4)	C(1)-N(1)-C(4): 117.3(2)
	N(1)-H(1A) : 0.8900	C(1)-N(1)-H(1A): 108.0
	N(1)-H(1B) : 0.8900	C(4)-N(1)-H(1A): 108.0
		C(1)-N(1)-H(1B): 108.0 C(4)-N(1)-H(1B): 108.0
		H(1A)-N(1)-H(1B): 107.2
		N(1)-C(1)-C(2): 107.8(3)
		N(1)-C(1)-C(3): 110.7(3)
		N(1)-C(1)-H(1): 109.0
		N(1)-C(4)-C(5): 107.5(3)
		N(1)-C(4)-C(6): 110.1(3)
		C(5)-C(4)-C(6): 112.4(3)
		N(1)-C(4)-H(4): 108.9
DIPA·BNPP (298 K)	P(1)-O(2) : 1.474(4)	O(2)-P(1)-O(1): 121.8(2)
	P(1)-O(1) : 1.486(5)	O(2)-P(1)-O(4): 106.4(2)
	P(1)-O(4) : 1.600(4)	O(1)-P(1)-O(4): 108.6(2)
	P(1)-O(3) : 1.618(5)	O(2)-P(1)-O(3): 110.1(2)
	O(3)-C(11) : 1.394(8)	O(1)-P(1)-O(3): 104.9(3)
	O(4)-C(21) : 1.400(7)	O(4)-P(1)-O(3): 103.7(3)
	O(11)-N(11) : 1.213(16)	C(11)-O(3)-P(1): 122.5(4)
	O(12)-N(11) : 1.174(15)	C(21)-O(4)-P(1): 121.0(4)
	N(1)-C(4) : 1.508(8)	C(4)-N(1)-C(1): 117.2(6)
	N(1)-C(1) : 1.513(8)	C(4)-N(1)-H(1A): 108.0
	N(1)-H(1A) : 0.8900	C(1)-N(1)-H(1A): 108.0
	N(1)-H(1B) : 0.8900	N(1)-C(4)-H(4): 109.0
		C(4)-N(1)-H(1B): 108.0
		C(1)-N(1)-H(1B): 108.0
		H(1A)-N(1)-H(1B): 107.2
		C(2)-C(1)-N(1): 110.7(7)
		N(1)-C(1)-C(3): 106.7(6)
		N(1)-C(1)-H(1): 109.4
		C(6)-C(4)-N(1): 111.1(7)
		C(5)-C(4)-N(1): 107.5(6)

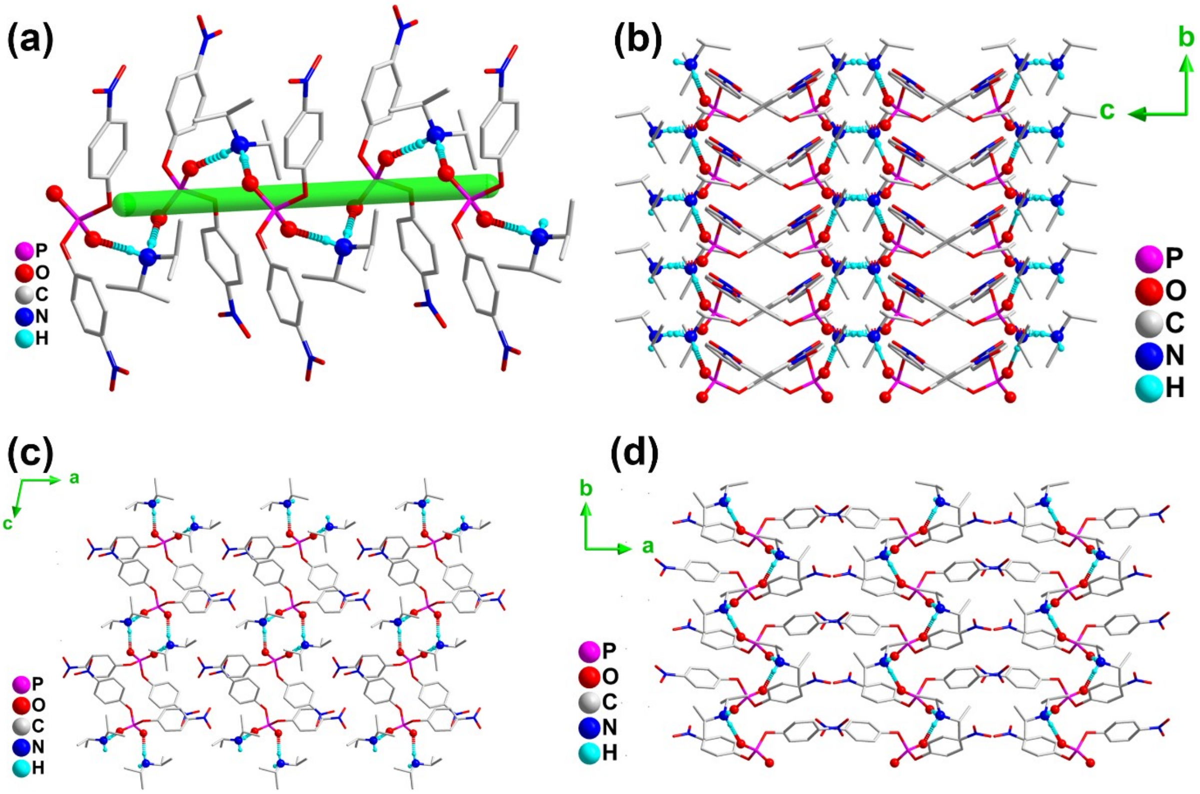

Figure S5: (a) H-bonding forms the helical structure along the b direction. (b) H-bonding packing diagram of **DIPA·BNPP** along *a*-axis. (b) H-bonding packing diagram of **DIPA·BNPP** along the *b*-axis. (c) H-bonding packing diagram of **DIPA·BNPP** along the *c*-axis.

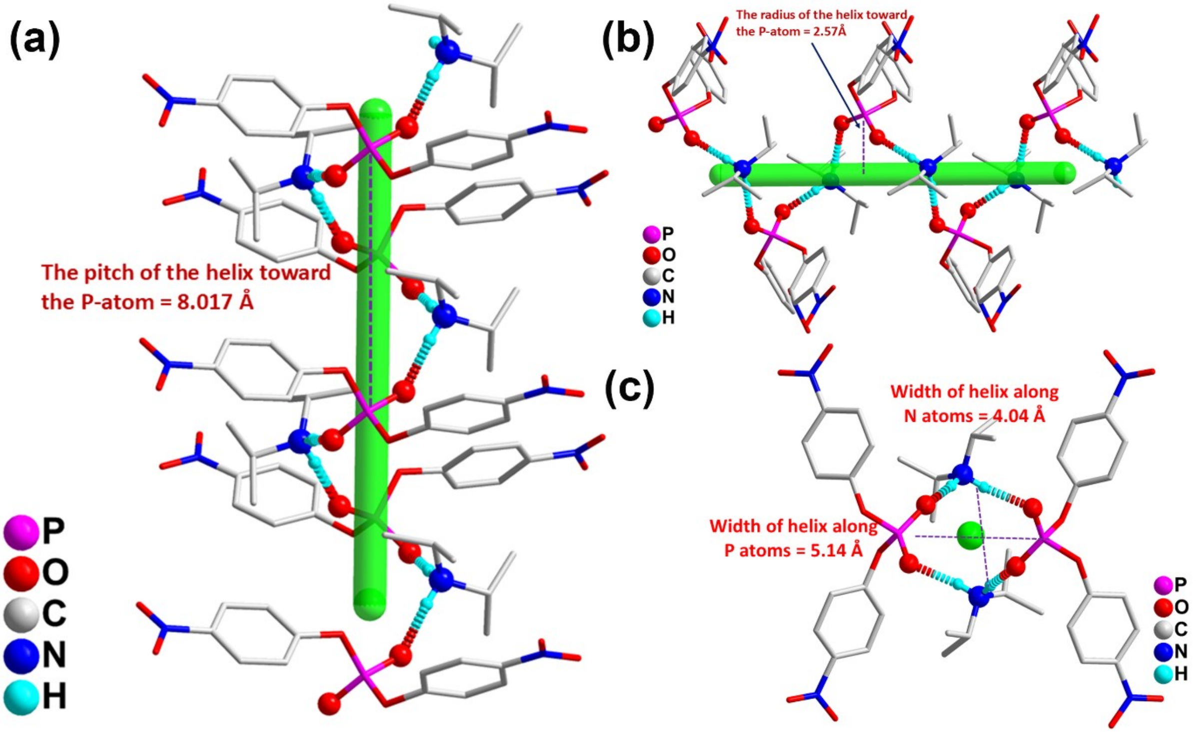

The pitch of the helix toward the P-atom = 8.017 Å

The radius of the helix toward the P-atom = 2.57Å

Width of helix along N atoms = 4.04 Å

Width of helix along P atoms = 5.14 Å

Figure S6: The structure adopts a helical arrangement along the b-axis, forming a ladder-like configuration. (a) The pitch of the helix is determined from P-atom to P-atom. (b) The radius of the helix is measured from the principal axis to the nitrogen atom. (c)The radius of the helix is measured from the principal axis to the phosphorous atom.

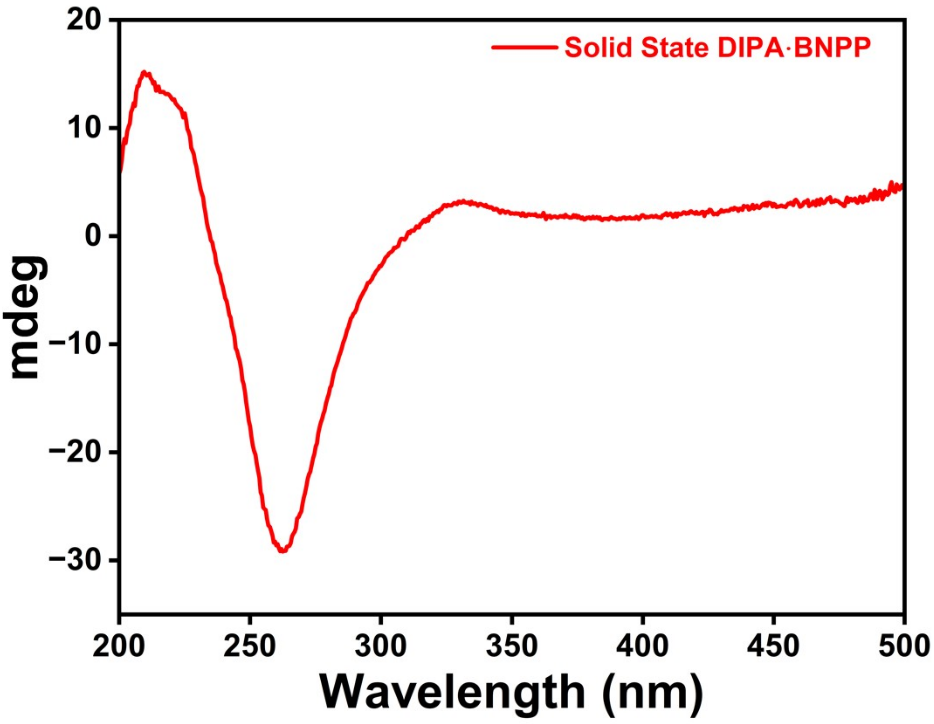

Figure S7: CD spectra of **DIPA·BNPP** in solid phase.

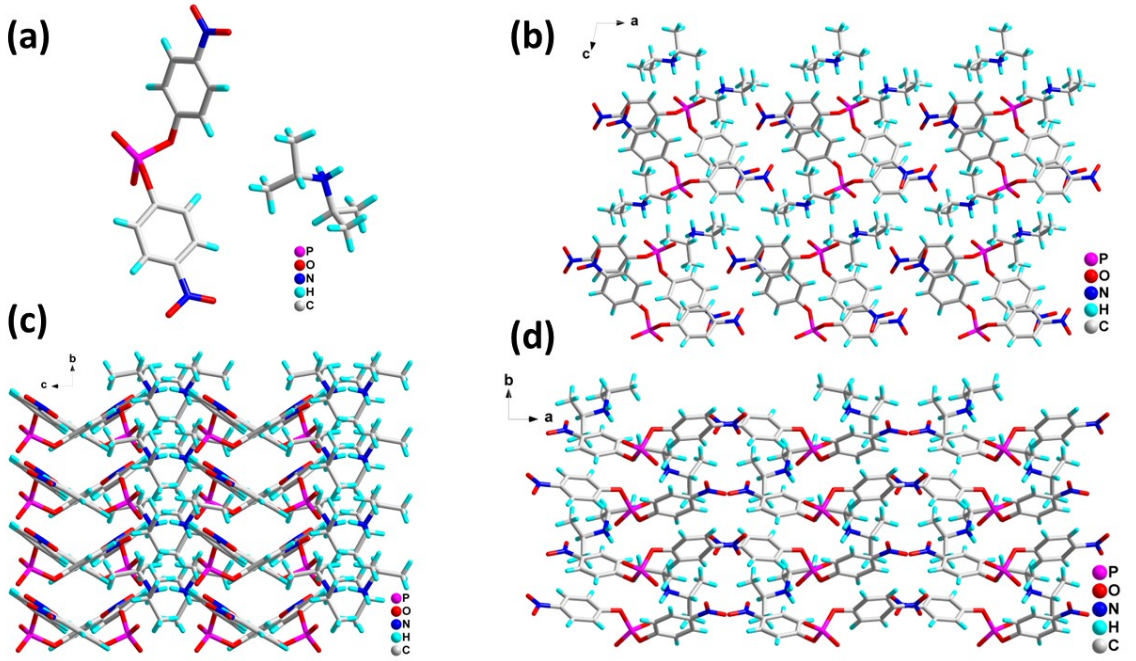

Figure S8. Packing diagrams of **DIPA·BNPP** at 150 K. (a) Asymmetric Unit of **DIPA·BNPP**. (b) Packing along *c* direction. (b) Packing along *a* direction. (c) Packing diagram of **DIPA·BNPP** along *b* direction.

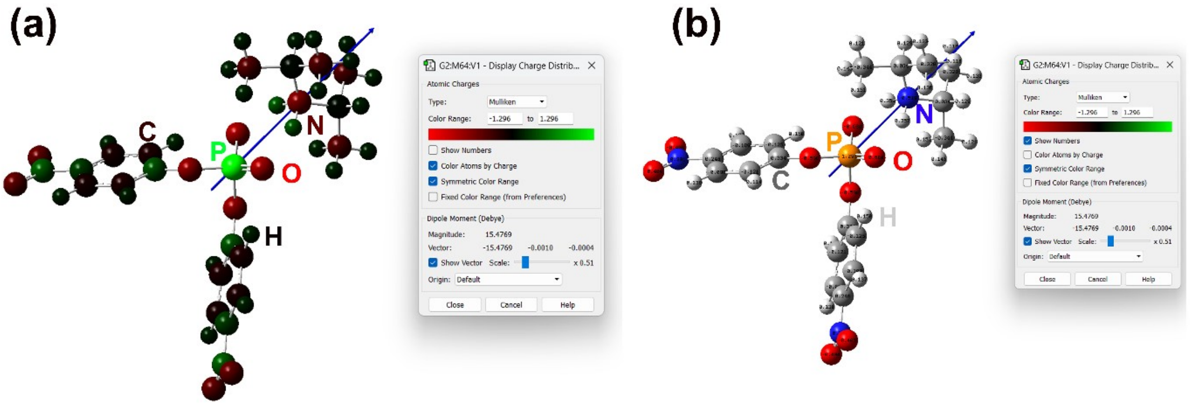

(a)

Atomic Charges
Type: Mulliken
Color Range: -1.296 to 1.296
☐ Show Numbers
☑ Color Atoms by Charge
☑ Symmetric Color Range
☐ Fixed Color Range (from Preferences)

Dipole Moment (Debye)
Magnitude: 15.4769
Vector: -15.4769 -0.0010 -0.0004
☑ Show Vector Scale: x 0.51
Origin: Default

(b)

Atomic Charges
Type: Mulliken
Color Range: -1.296 to 1.296
☑ Show Numbers
☐ Color Atoms by Charge
☑ Symmetric Color Range
☐ Fixed Color Range (from Preferences)

Dipole Moment (Debye)
Magnitude: 15.4769
Vector: -15.4769 -0.0010 -0.0004
☑ Show Vector Scale: x 0.51
Origin: Default

Figure S9. (a) Dipole-moment vector direction (shown as arrows, Table S3) and Mulliken atomic charge maps for **DIPAP.BNPP**. Color code: C, dark maroon; H, black; P, green; O, red; N, maroon. (b) Dipole-moment vector direction (shown as arrows) and Mulliken atomic charge number given for **DIPA·BNPP** (For more details, refer to Table S4).

Table S3. Table for the dipole moment obtained from the independent field by DFT calculation.

Dipole moment (debye)	x-axis	y-axis	z-axis	Total
Dipole moment at 298 K	-15.4769	-0.0010	-0.0005	15.4769

Table S4. Table for the Mulliken charges with hydrogens summed into heavy atoms.

Serial No.	atoms	Mulliken charges
1	P	2.832847
2	O	-1.395135
3	N	1.304660
4	O	-1.395160
5	O	-1.167886
6	O	-0.679016
7	O	-0.673794
8	O	-0.679020
9	O	-0.673796
10	N	1.304660
11	C	0.841268
12	O	-1.167954
13	C	-0.171162
14	C	0.190730
15	C	0.190730
16	C	-0.287553
17	C	-0.287553
18	C	-0.124233
19	C	0.841246
20	C	-0.124222
21	C	0.208168
22	C	-0.287568
23	C	0.190739
24	C	-0.171172
25	N	0.267602
26	C	0.044021
27	C	0.346664
28	C	0.013105
29	C	0.013121
30	C	0.346644
31	C	0.044017
32	C	-0.124233

33	C	0.841246
34	C	-0.124222

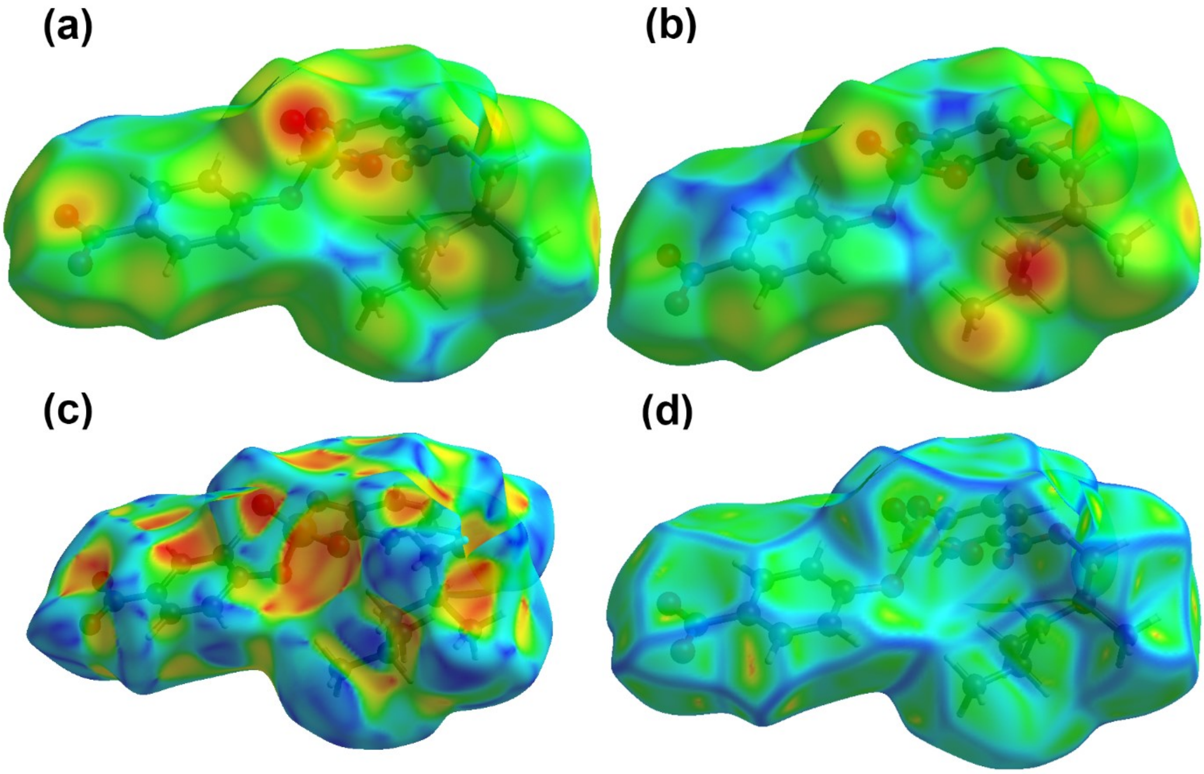

Figure S10. The 3D colour mapping obtained from the Hirshfeld surface analysis of **DIPA·BNPP** at 298 K illustrates the following features: (a) d_i, (b) d_e, (c) shape index, and (d) curvedness.

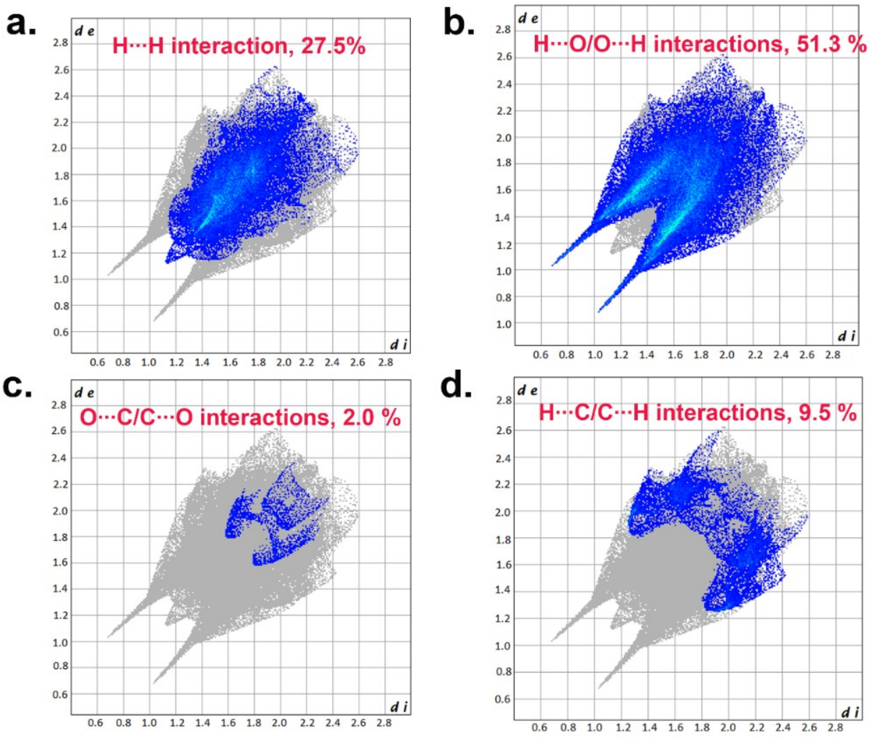

Figure S11. 2D fingerprint (d_e vs. d_i) plots of **DIPA·BNPP** (150 K) showing the percentages of (a) H···H, (b) O···H/H···O, (c) O···C/C···O, (d) C···H/H···C interactions.

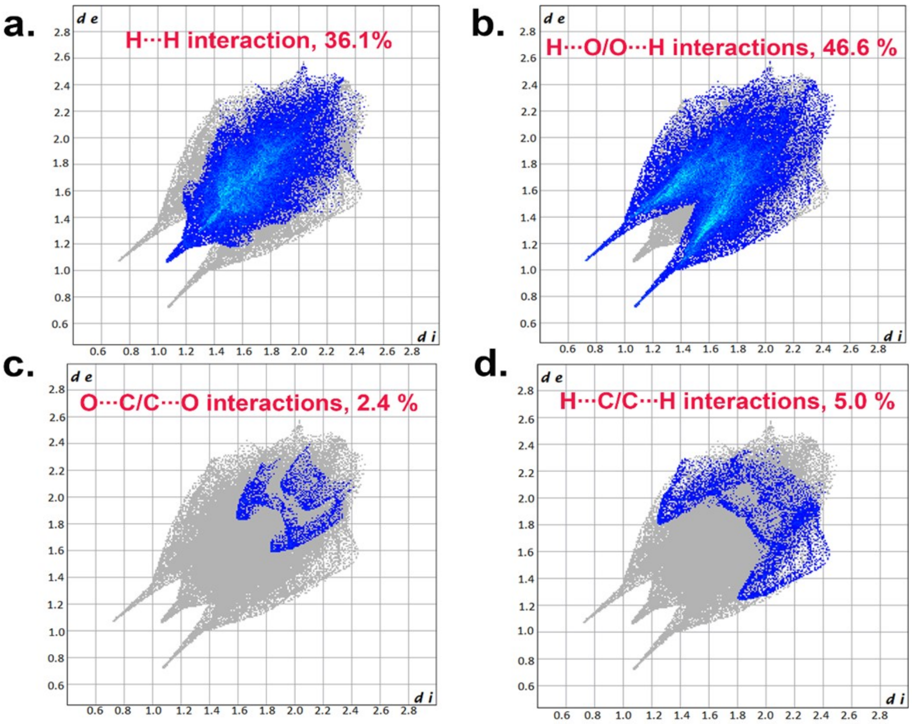

Figure S12. 2D fingerprint (d_e vs. d_i) plots of **DIPA·BNPP** (298 K) showing the percentages of (a) H···H, (b) O···H/H···O, (c) O···C/C···O, (d) C···H/H···C interactions.

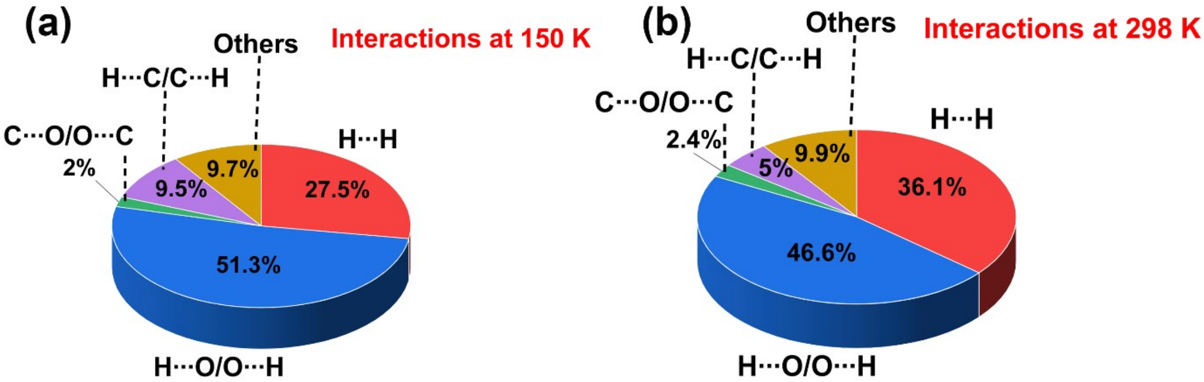

Figure S13. 3D-Pie graph of all types of percentage Interactions presents in **DIPA·BNPP**. (a) 3D-Pie graph of all types of percentage Interactions presents in **DIPA·BNPP** at 150 K (b) 3D-Pie graph of all types of percentage Interactions present in **DIPA·BNPP** at 298 K.

Table S5. Hirshfeld surface analysis of **DIPA·BNPP** at 150 K and 298 K.

Compound	Temperature	Surface Property	Range (minimum/maximum)	Globularity and Asphericity	Surface Volume and Area
DIPA·BNPP	**150 K**	d_i	0.6765/2.6155	0.675 and 0.118	523.42 Å^3 and 465.39 Å^2
		d_e	0.6763/1.6930		
		d_{norm}	-0.6763/1.5410		
		Curvedness	-3.8785/0.2998		
		Shape Index	-0.9969/0.9964		

DIPA·BNPP RT	**298 K**	d_i	0.7319/2.5177	0.733 and 0.156	542.01Å^3 and 438.56 Å^2
		d_e	0.7304/2.6214		
		d_{norm}	-0.6172/1.5984		
		Curvedness	-0.4.2555/0.4536		
		Shape Index	-0.9927/0.9973		

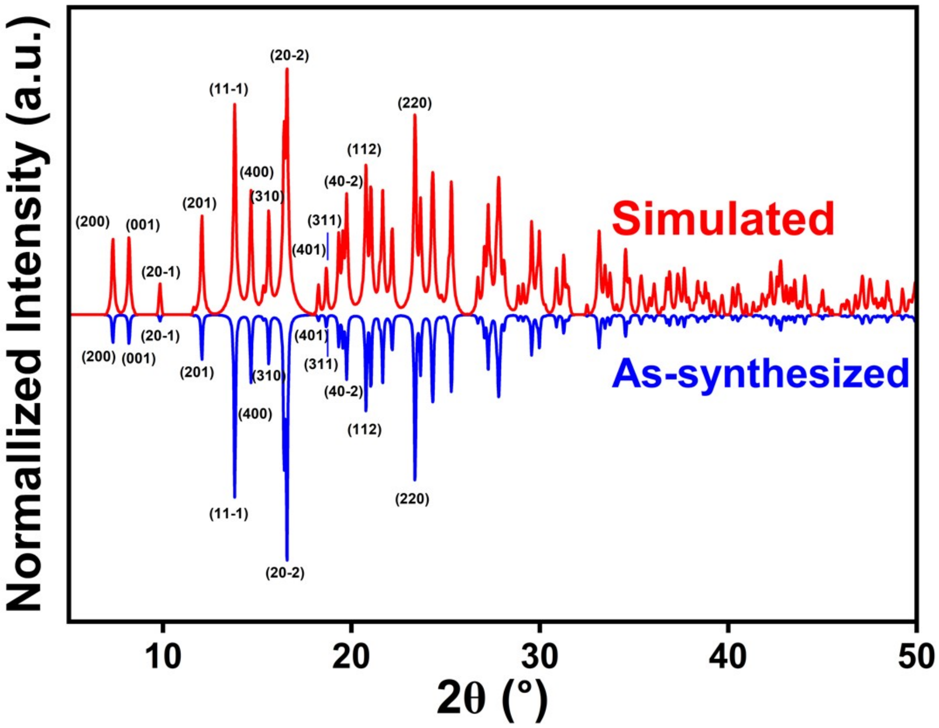

Figure S14. The PXRD spectrum of simulated and as-synthesized **DIPA·BNPP**.

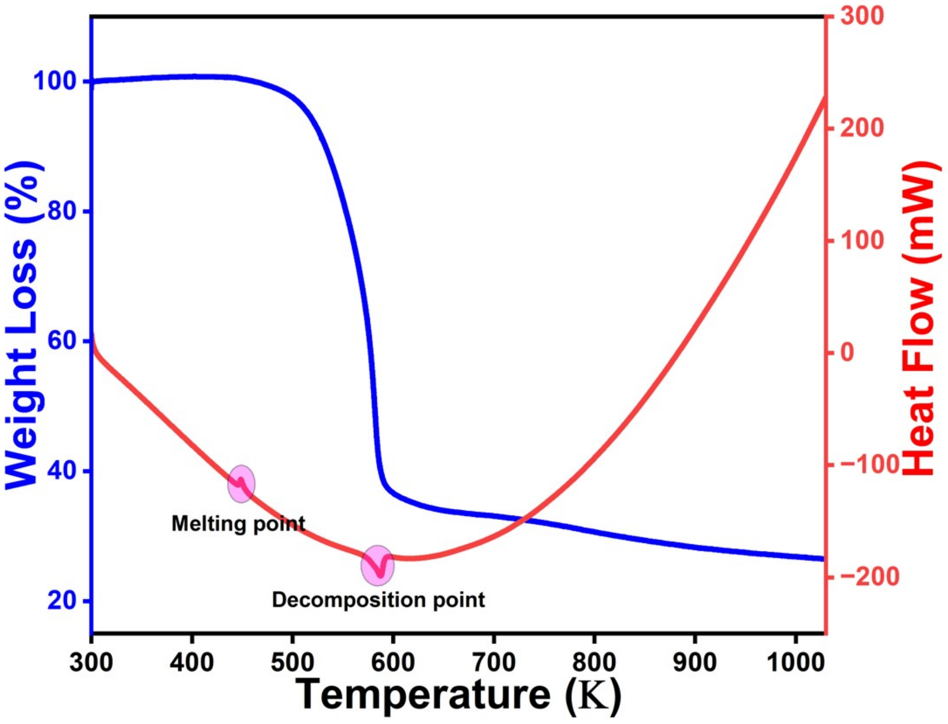

Figure S15. TGA and DTA profile diagram of **DIPA·BNPP**.

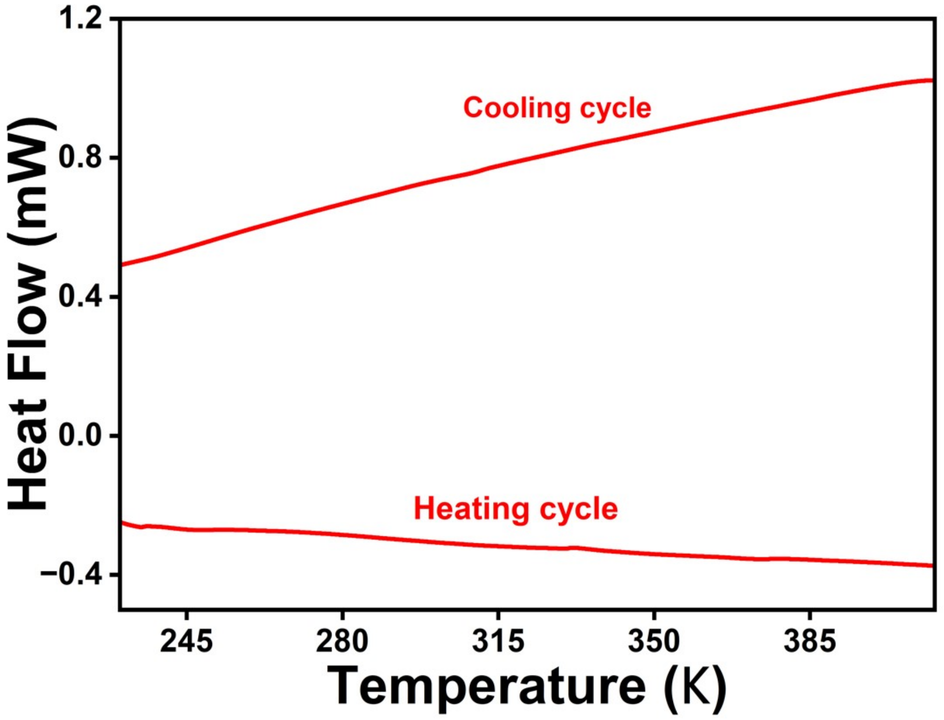

Figure S16. Differential scanning calorimetry (DSC) analysis of **DIPA·BNPP**.

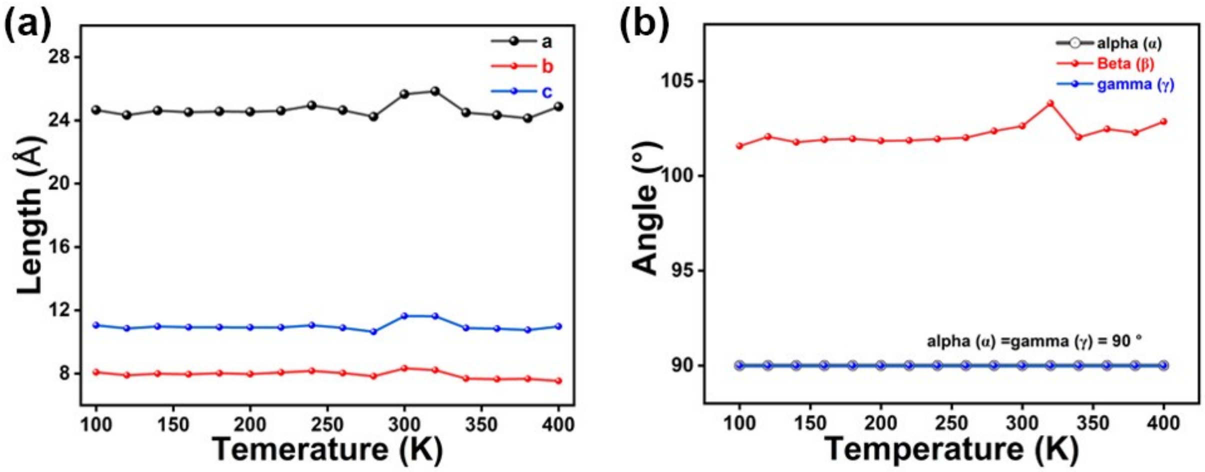

Figure S17. Variable temperature unit cell parameter determination from the SCXRD. (a) Unit cell a, b, c. parameter (b) Unit cell angle α, β, γ.

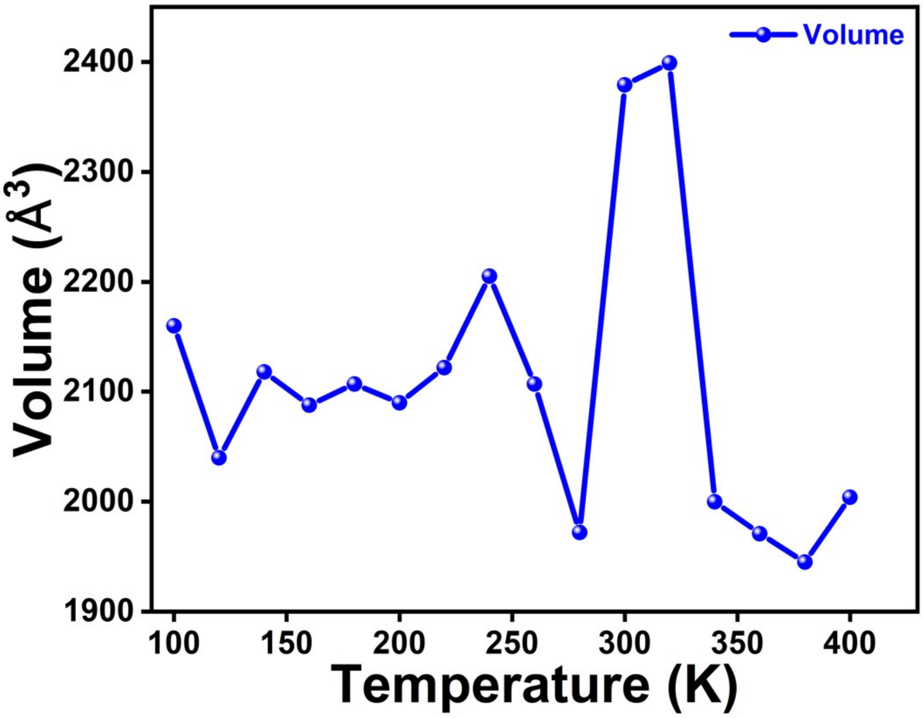

Figure S18. Variable temperature unit cell volume determination of **DIPA·BNPP** from the SCXRD data.

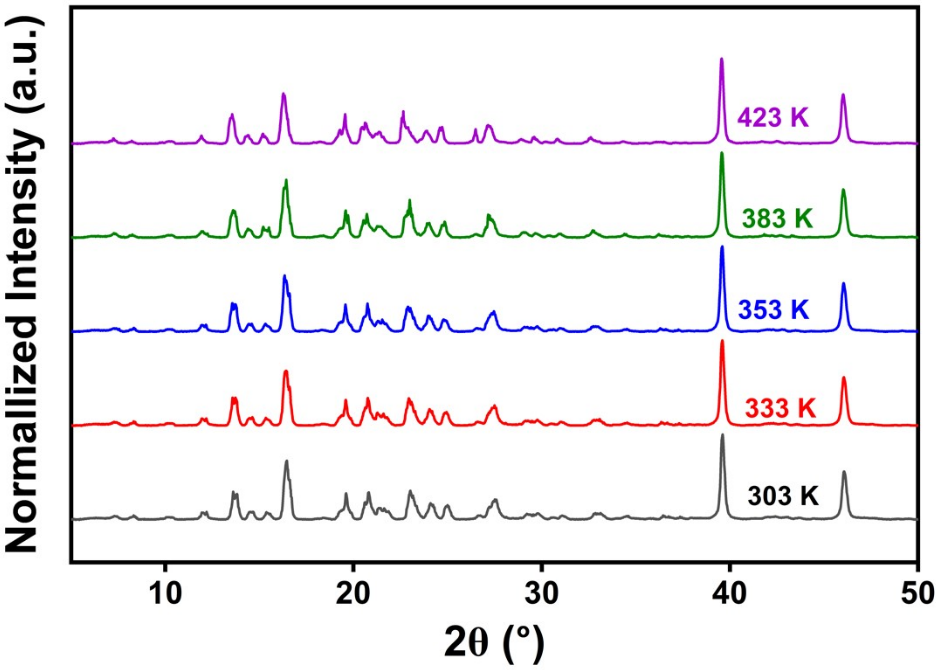

Figure S19. The variable-temperature PXRD data of **DIPA·BNPP**.

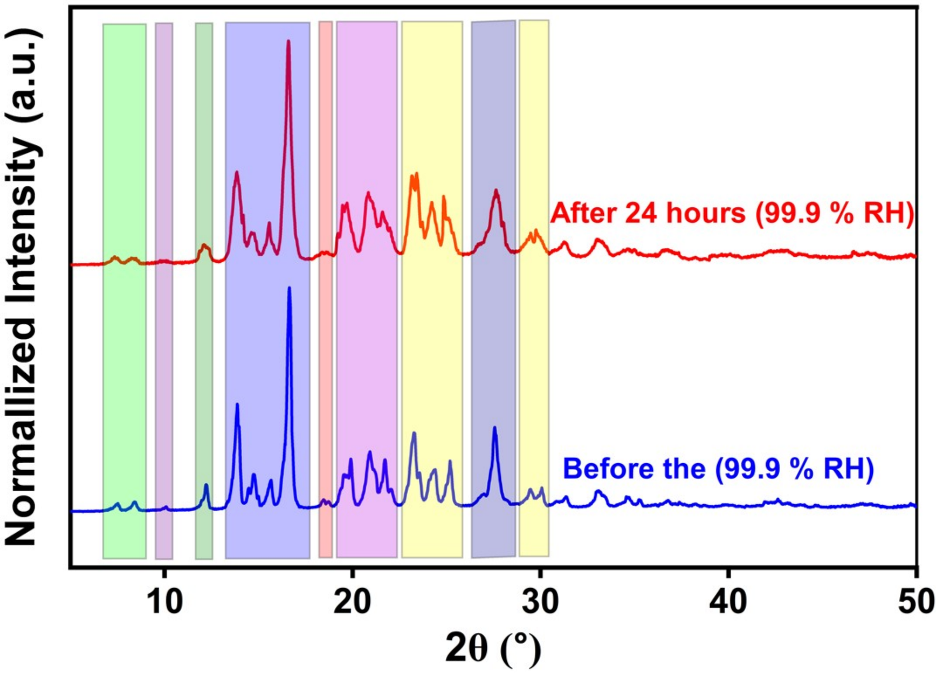

Figure S20. Humidity-dependent PXRD before the 99.9% humidity and after 99.9% humidity, after 24 hours.

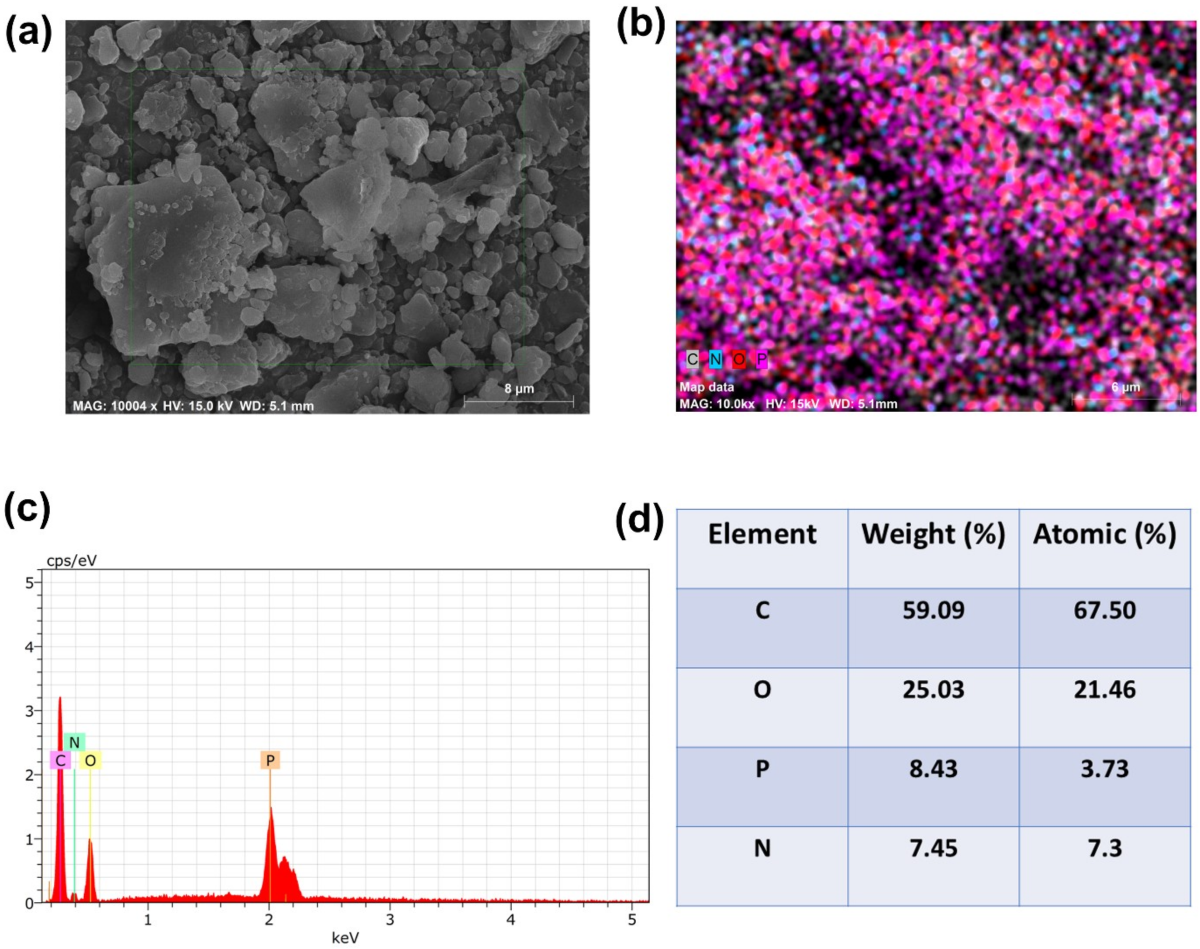

Element	Weight (%)	Atomic (%)
C	59.09	67.50
O	25.03	21.46
P	8.43	3.73
N	7.45	7.3

Figure S21. (a) FE-SEM image of **DIPA·BNPP** was used for the elemental composition analysis. (b) Elemental composition colour mapping image. (c) and (d) Energy-dispersive X-ray spectroscopy (EDXS) analysis showing the quantitative elemental composition of C, N, P, and O (EDXS data shown here was an average of 4 measurements). The powdered sample of **DIPA·BNPP** was used for the analysis.

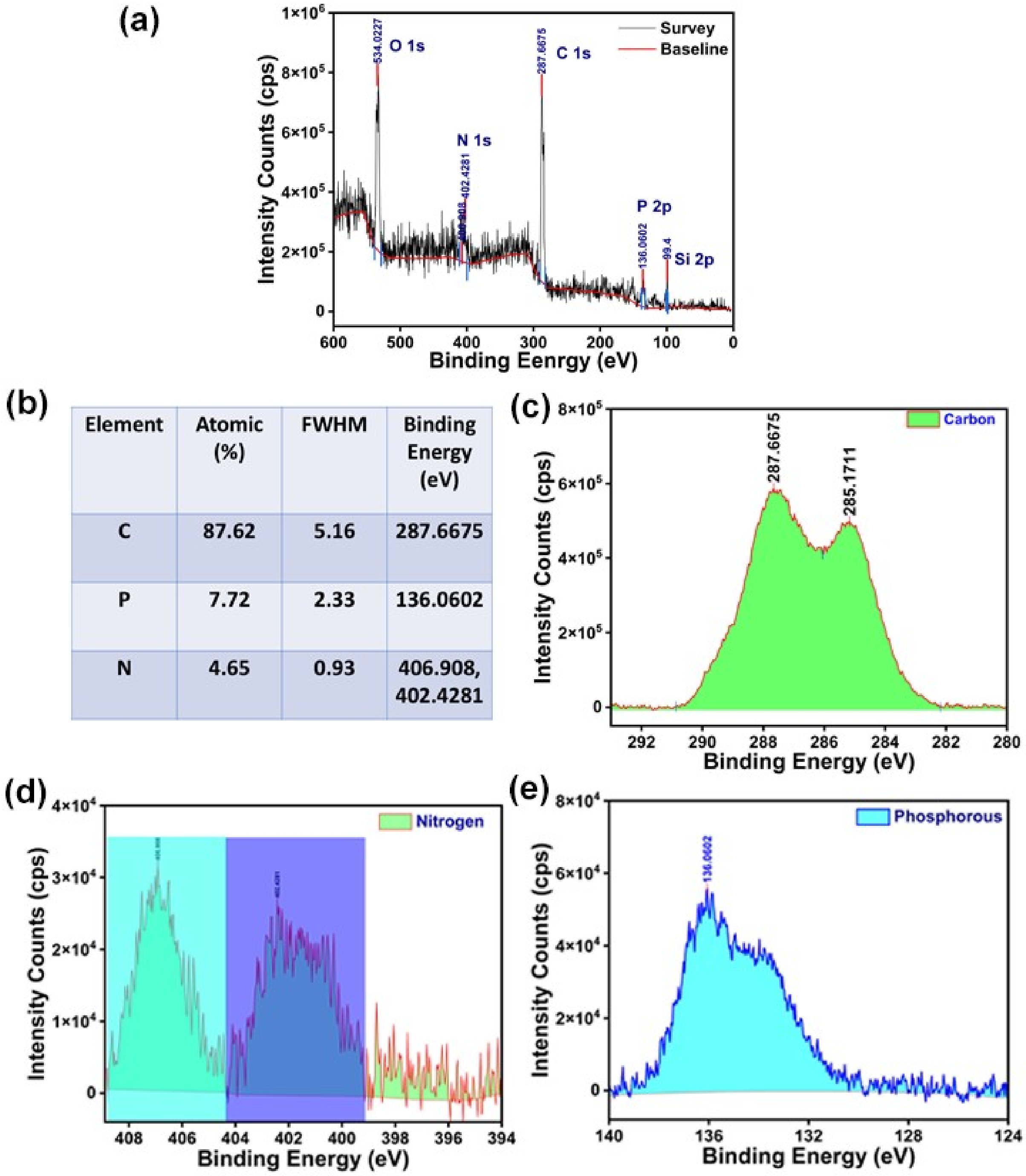

Element	Atomic (%)	FWHM	Binding Energy (eV)
C	87.62	5.16	287.6675
P	7.72	2.33	136.0602
N	4.65	0.93	406.908, 402.4281

Figure S22: (a) XPS Survey Spectra of **DIPA·BNPP**. (b) Atomic composition and binding energy of atoms in **DIPA·BNPP**. High-resolution XPS spectra of (c) C 1s, (d) N 1s and (e) P 2p of **DIPA·BNPP**.

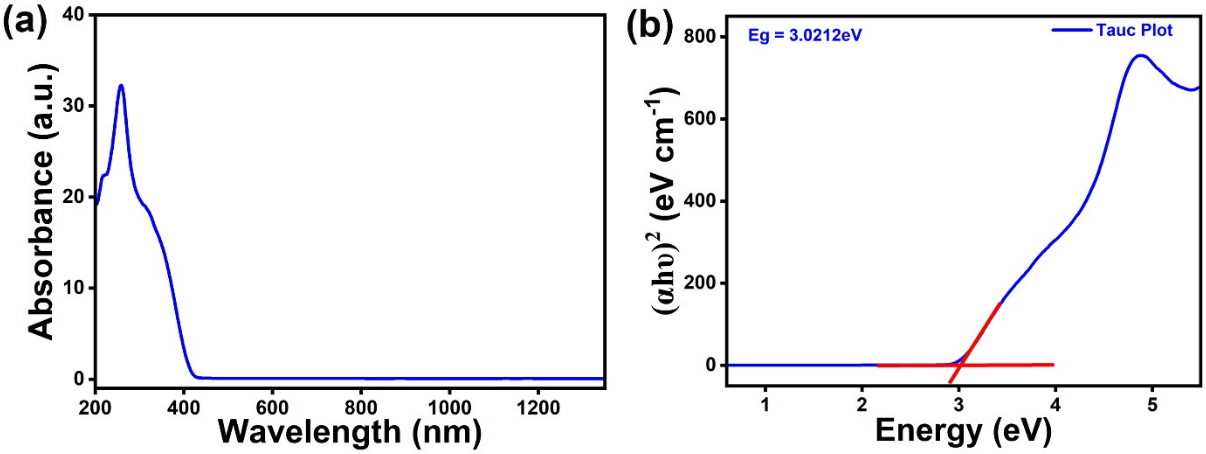

Figure S23. (a) Solid state UV spectrum and (b) the tauc plot of **DIPA·BNPP**.

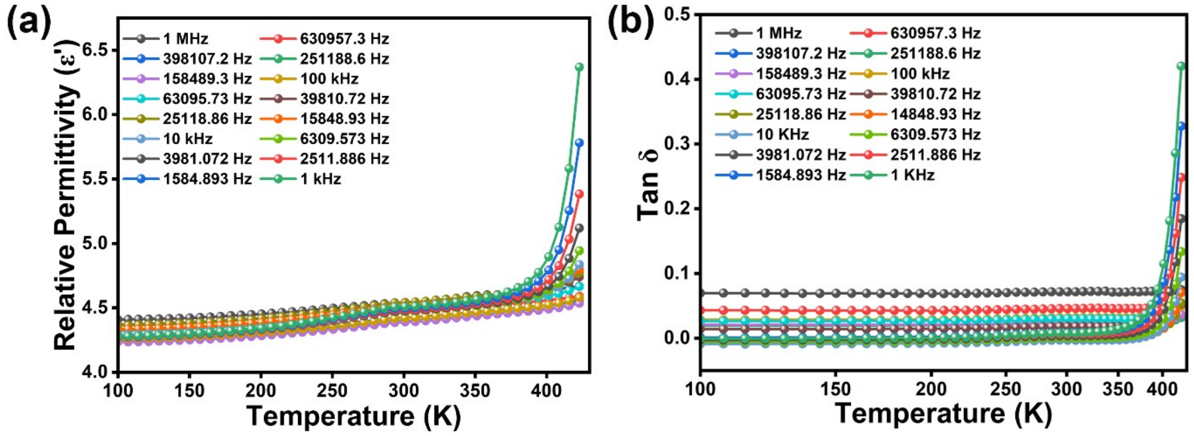

Figure S24. (a) The real part of dielectric permittivity versus temperature profile of **DIPA·BNPP**. (b) The dielectric loss factor (tan δ) versus temperature profile of **DIPA·BNPP**.

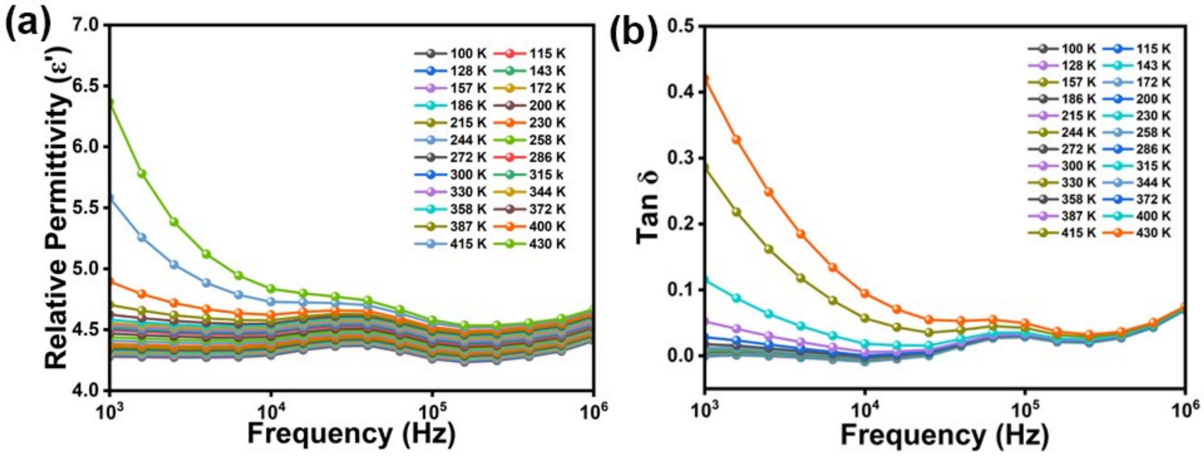

Figure S25. (a) Dielectric permittivity versus frequency profile of **DIPA·BNPP** at various temperatures. (b) Dielectric loss factor (tan δ) versus frequency profile of **DIPA·BNPP** at various temperatures.

.

Figure S26. The d_{33} value for a poled, compacted pellet of **DIPA·BNPP**.

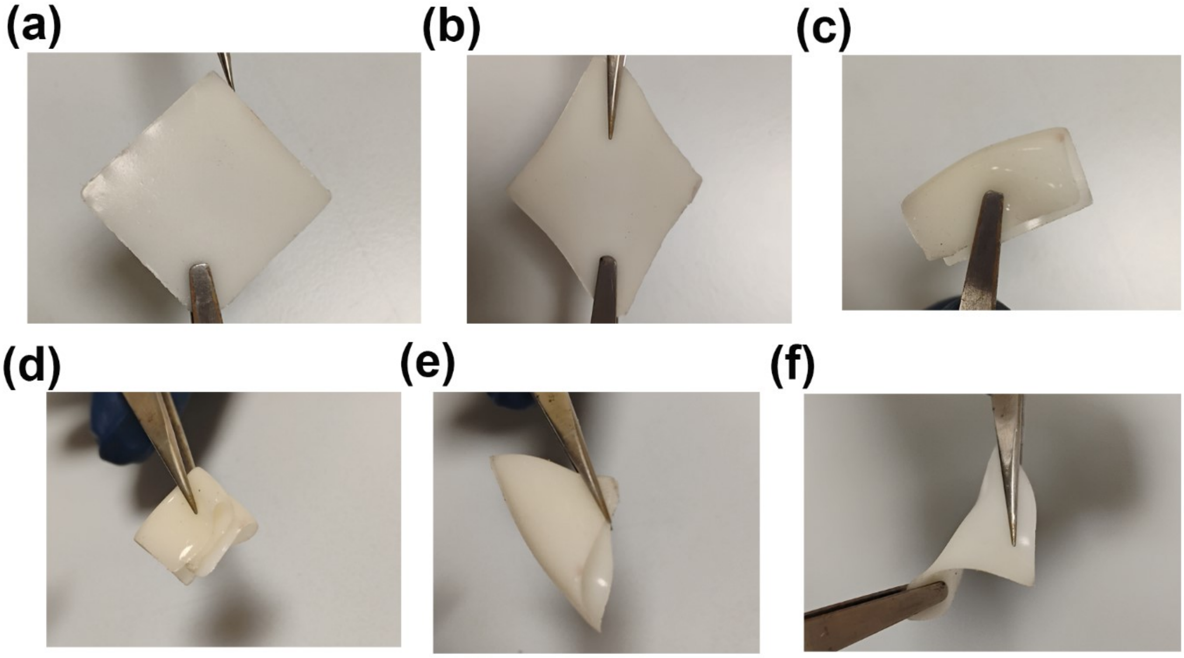

Figure S27. Photograph of a representative (a) as-made composite film of **DIPA·BNPP-**PDMS showing its flexibility towards (b) Diagonal stretching, (c) Two-fold folding, (d) Four-fold folding, (e) Diagonal folding, (f) Twisting operations.

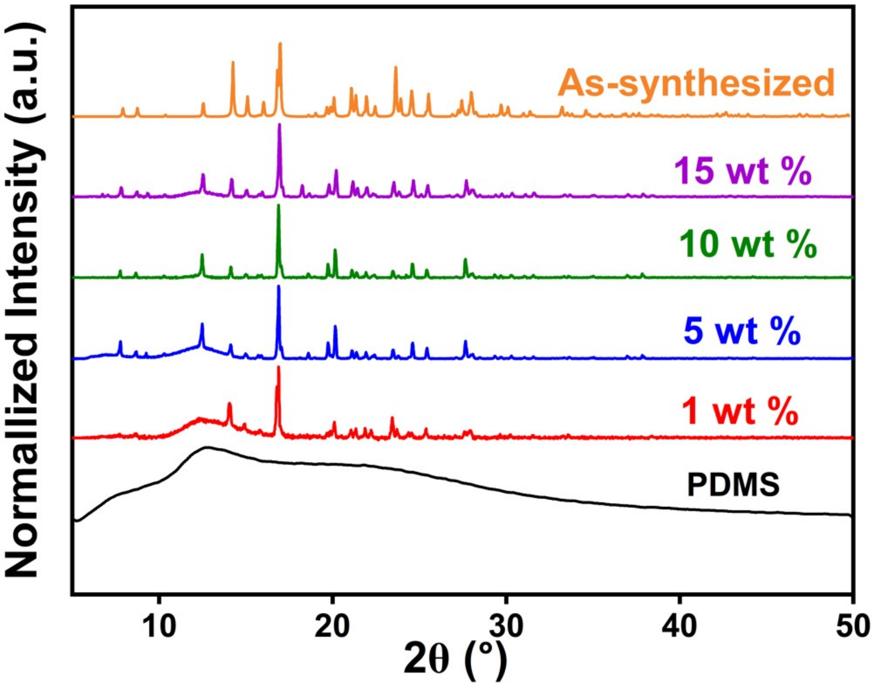

Figure S28. PXRD profiles of various weight percentages (1 wt%, 5 wt%, 10 wt%, 15 wt%) of **DIPA·BNPP**-PDMS composite films, and its comparison with pristine **DIPA·BNPP**-PDMS shows the stability of **DIPA·BNPP**-PDMS inside the PDMS matrix.

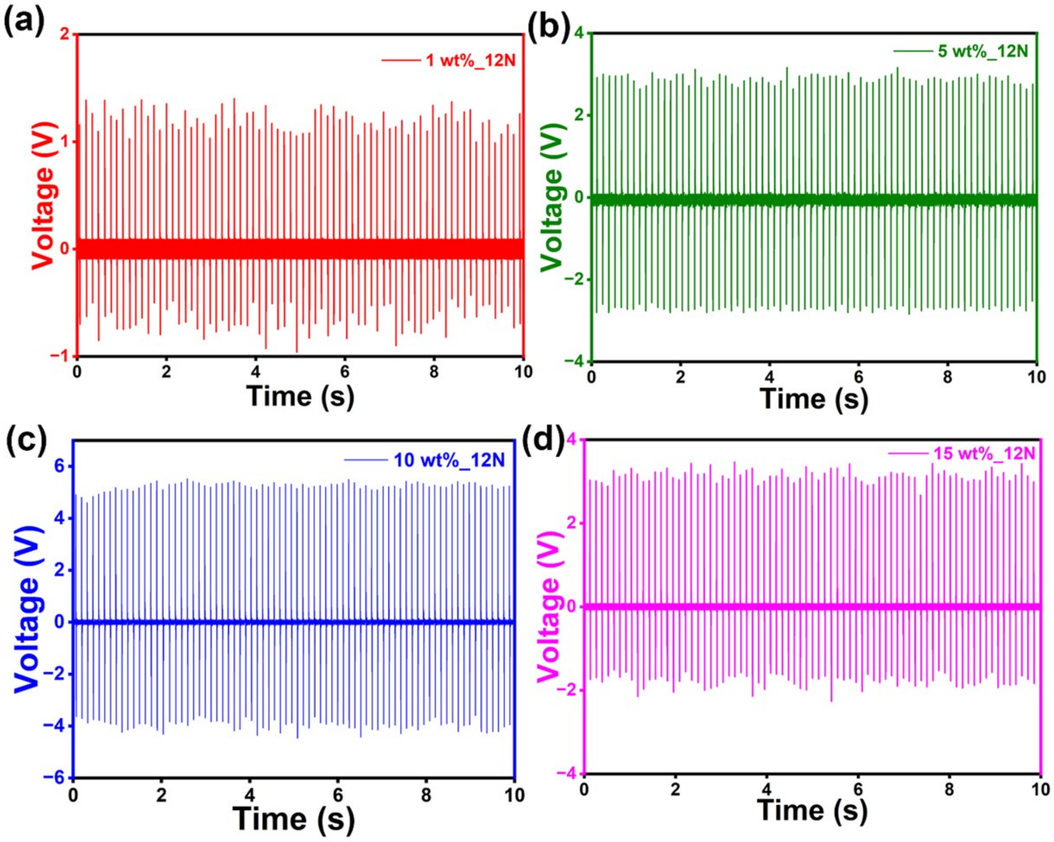

Figure S29. The piezoelectric output, open-circuit voltages of the various wt% of **DIPA·BNPP**-PDMS PENG devices (a) 1 wt% (b) 5 wt% (c) 10 wt% (d) 15 wt%.

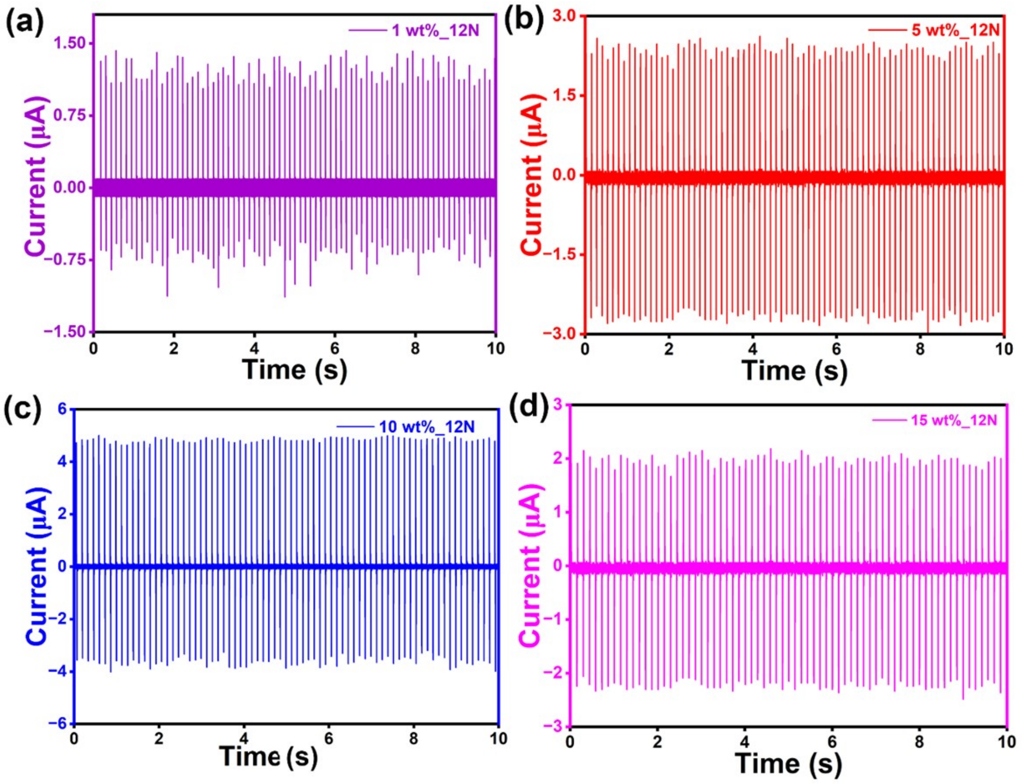

Figure S30. The piezoelectric output, open-circuit current of the various wt% of **DIPA·BNPP**-PDMS PENG devices (a) 1 wt% (b) 5 wt% (c) 10 wt% (d) 15 wt%.

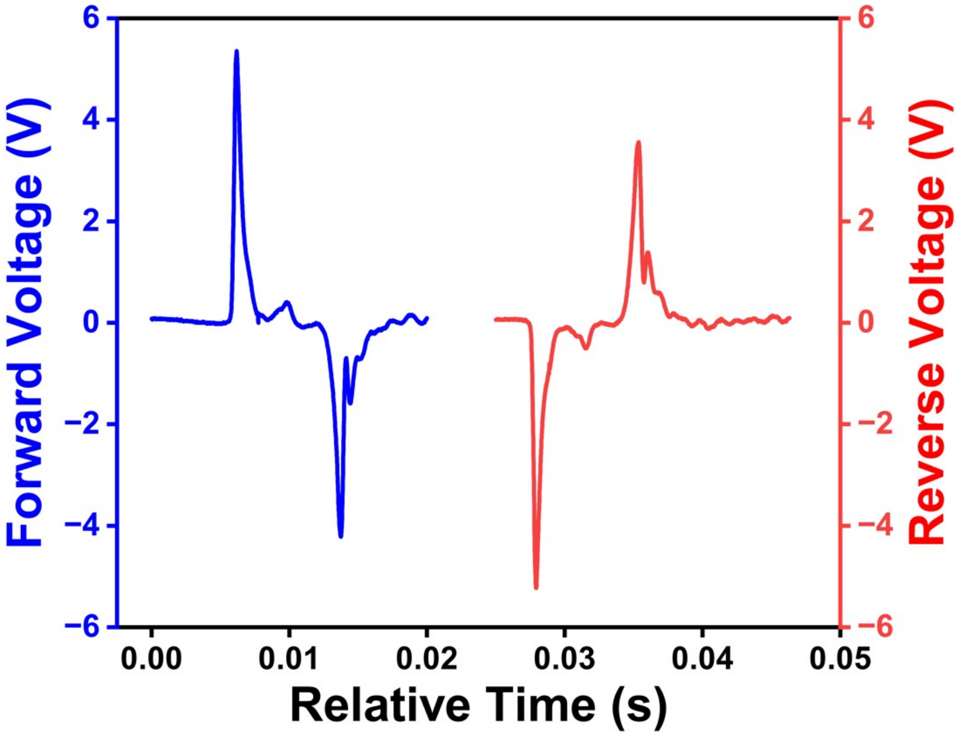

Figure S31. Reverse and forward connection peak to peak voltage of the 10 wt% DIPAP·BNPP-PDMS device under the 12 N force.

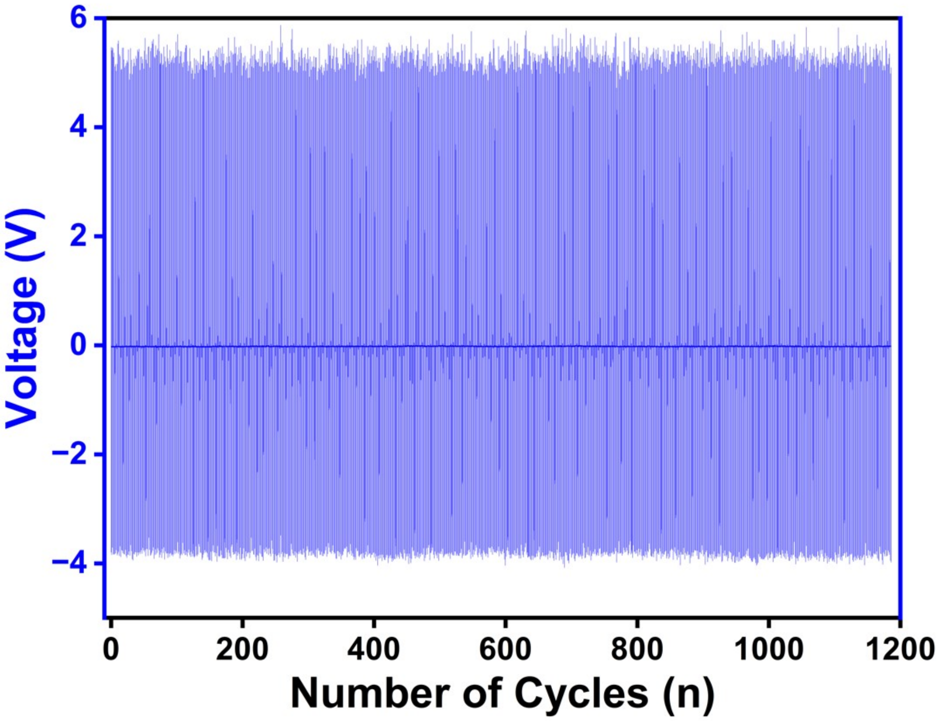

Figure S32. The cyclic stability of the 10 wt% **DIPA·BNPP**-PDMS device was tested after approximately 3 months under 12 N force.

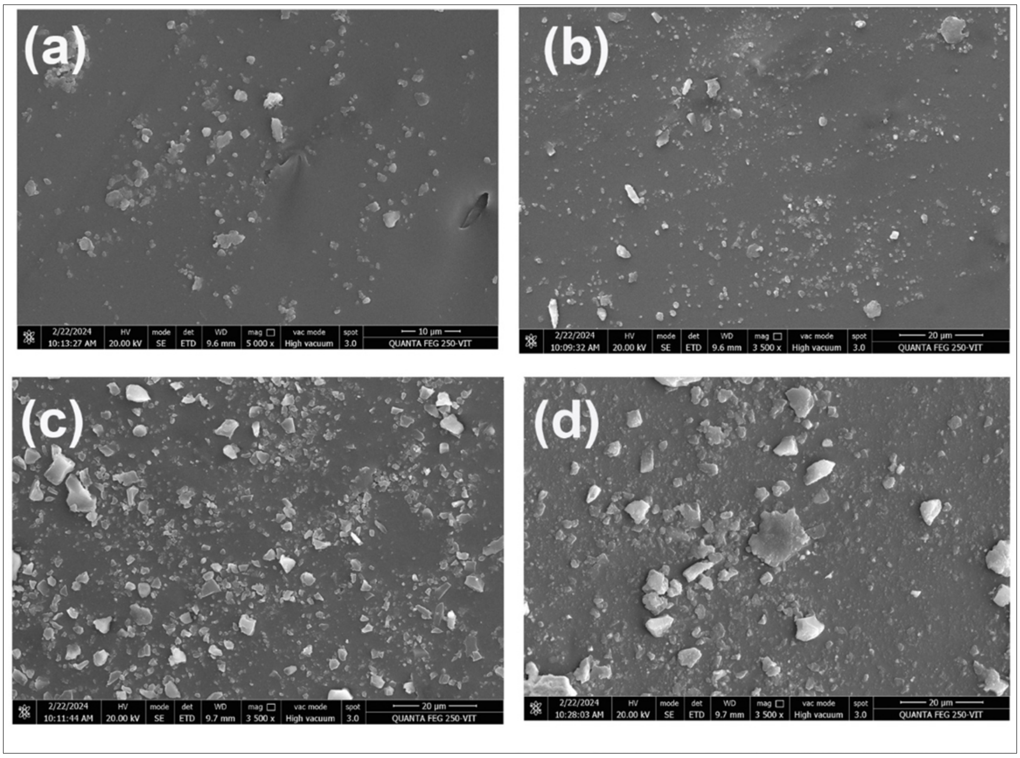

Figure S33. (a) The FE-SEM images of different weight percentages PDMS composite films of **DIPA·BNPP** (a) 1 wt% (b) 5 wt% (c) 10 wt% (d) 15wt%.

Supporting discussion 1: In our experimental setup, the force measurement is inherently independent and cannot be directly controlled. However, we can adjust the effective force by varying the vertical distance between the sample holder and the impact system. This height adjustment is achieved by introducing a thin iron plate beneath the sample holder, as depicted in Figure 34, which effectively alters the distance between the sample holder and the impact mechanism. By decreasing this distance, the force exerted on the sample increases. This method allows for precise modulation of the force applied during the measurement process.

To ensure precise measurement of the applied force and the effective working area, the experimental setup has been meticulously aligned in a collinear configuration. Distinct areas have been designated for the sample holder, the piezoelectric nanogenerator (PENG) device, and the impact system to optimize measurement sensitivity, operational frequency, and force transfer efficiency, as illustrated in Figure S34 b. This structural configuration enhances both the consistency and reproducibility of the experimental results. A detailed schematic diagram of the setup has been provided for clarity.

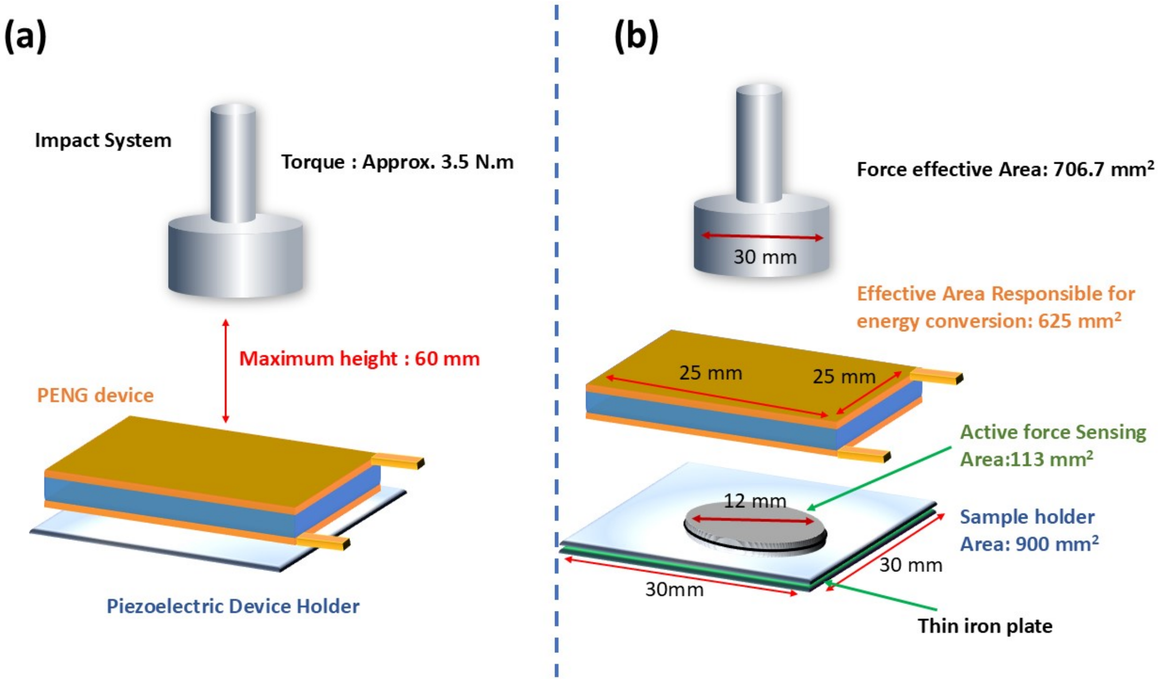

Figure S34. (a)Schematic of the force-dependent measurement setup (b) Schematic representation of the force sensor.

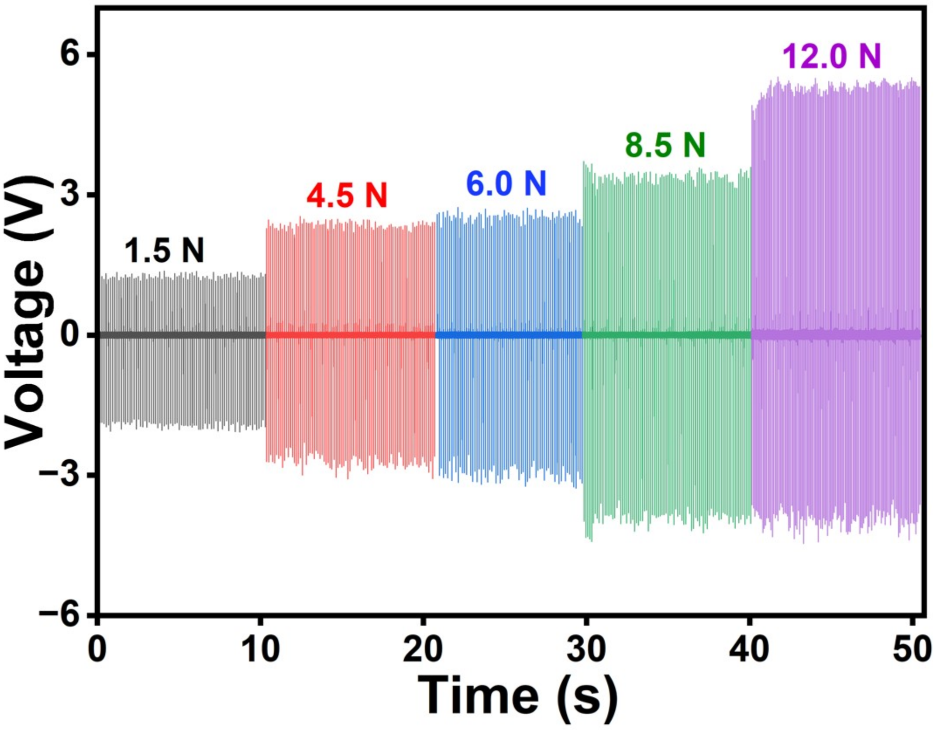

Figure S35. Force dependent piezoelectric open circuit output voltage of 10 wt% **DIPA·BNPP**-PDMS device.

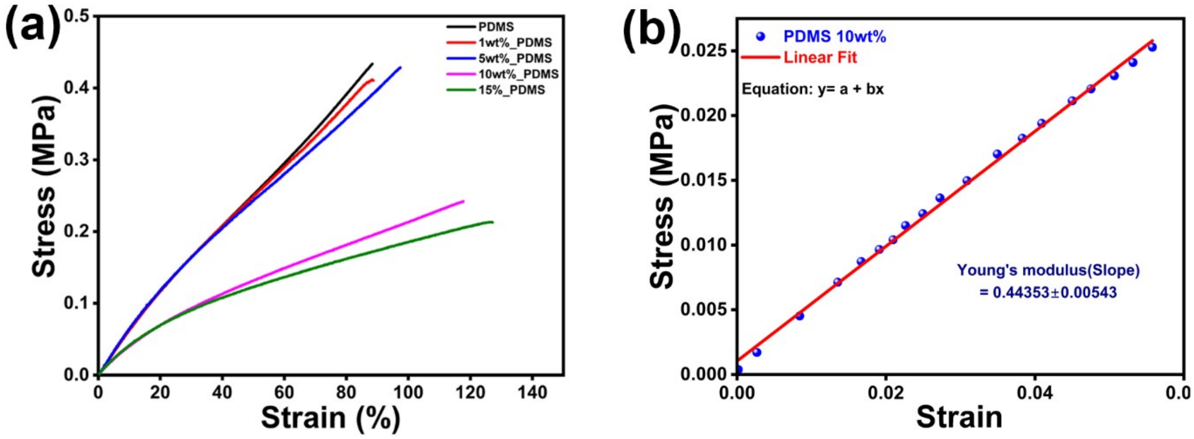

Figure S36. Strain-stress measurement of PDMS composite film **DIPA·BNPP**-PDMS. (a) Stress-strain percentage analysis for all the composite films. (b) stress-stain plots for the 10 wt % **DIPA·BNPP**-PDMS in the linear region.

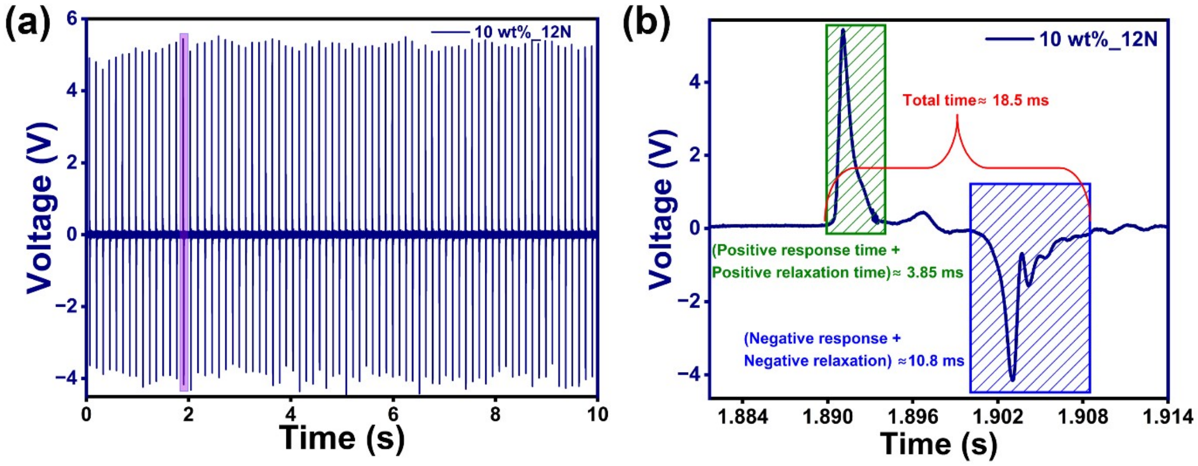

Figure S37. Pressure sensing characteristics of the 10 wt% **DIPA·BNPP**-PDMS PENG device under a load of 12 N. (a) Open circuit voltage of 10 wt% **DIPA·BNPP**-PDMS device (b) Enlarged large view of the positive and negative signal.

Supporting Discussion 2: Device Efficiency/ Work efficiency calculation:

The efficiency of a 10 wt% **DIPA·BNPP** PENG device can be calculated by taking the ratio of the output electrical energy of the device and the intrinsic elastic energy of the 10 wt% **DIPA·BNPP** composite film.

The intrinsic elastic deformation energy (U_d) is given by

$$U_d = \frac{1}{2} \times \frac{stress^2}{Young's\ modulus} \times volume\ of\ effective\ area$$

→Eqn. 1

Here, stress is the applied pressure obtained from the applied force on a unit area.[6] Application of 12N force on a 2.5 x 2.5 cm^2 device produces a pressure of 0.0192 MPa. From Figure S36 b, the corresponding Young's modulus is found to be 0.44353. The thickness of the device is 0.37 cm. Using these values, U_d is calculated to be $9.6 \times 10^{-2} Joule$ as per the below calculations.

$$U_d = \frac{1}{2} \times \frac{(0.0192\ MPa)^2}{0.44353\ MPa} \times (2.5\ cm \times 2.5\ cm \times 0.37\ cm)$$

$$U_d = \frac{1}{2} \times (0.0192)^2 \times 10^6\ N/m^2 \times \frac{1}{0.4705} \times (2.3125\ cm^3)$$

$$U_d = \frac{1}{2} \times (0.0192)^2 \times 10^6\ N/m^2 \times \frac{1}{0.44353} \times (2.3125 \times 10^{-6}\ m^3)$$

$$U_d = 9.6 \times 10^{-4}\ N.m$$

$$U_d = 9.6 \times 10^{-4}\ J$$

→Eqn. 2

Since the deformation energy per second (U_d/s) is the input work done (W_d) per second, the energy consumed by the device can be expressed as shown below.

$$W_d = \frac{U_d}{s_d} J/s$$

→ Eqn. 3

Where s_d is the deformation time for the composite film, which can be calculated as given below.

The frequency of the impact force from the home-built set-up (8 Hz), therefore the total time taken for one cycle of deformation and reformation of the composite is 125 ms ($\frac{1}{8}$ s). Of this 125 ms, the total time taken by the 10 wt% **DIPA·BNPP** device to produce one cycle of output peak-to-peak voltages (in the positive and negative directions) is calculated to be 18.5 ms. Of this (18.5 ms), the time taken for the positive half cycle is 3.85 ms, which is the time taken for the deformation of the device.[7] The remaining time is considered to be reformation time plus the time delay between the two half cycles (Figure S37 b). By taking the ratio between the deformation time and the total time (deformation + reformation + time delay) for producing one cycle of positive and negative signals produced by the 10 wt% **DIPA·BNPP** device and equating it to the frequency of the impact force set-up for producing one cycle of deformation and reformation (for 125 ms), the accurate deformation time (s_d) for one full cycle can be calculated as below.

$$s_d = \frac{3.85\ ms}{18.5\ ms} \times\ 125\ ms$$

$$s_d = 26.01\ \times\ 10^{-3}\ s \rightarrow \text{Eqn. 4}$$

Substituting the value of $U_d$from Eqn. 2 and the value of s_d from Eqn. 4 in Eqn. 3, we get the input work done (W_d) per second as below

$$W_d = \frac{9.6\ \times 10^{-4}}{26.01\ \times\ 10^{-3}} Js^{-1}$$

$$W_d =\ 3.696\ \times\ 10^{-2} Js^{-1} \rightarrow \text{Eqn. 5}$$

Similarly, the output electrical energy (U_e) can be obtained from the output voltage and calculated current of the device in unit time

$$U_e = V \times i \times t \rightarrow \text{Eqn. 6}$$

From Figure S28b, the total time taken to produce one cycle of output peak-to-peak voltages (in the positive and negative directions) is calculated to be 18.5 ms. For one cycle, the maximum peak-to-peak voltage is 9.5 V, and the corresponding current is calculated to be 9.424 µA. The output electrical energy (U_e) generated in one millisecond (ms) can be expressed as

$$U_e = 9.5\ V \times (9.424 \times 10^{-6}\ A) \times \left(\frac{1}{18.5}\right) ms$$

Therefore, the output electrical energy (U_e) generated in one second (s) can be given by

$$U_e = 9.5\ V \times (9.424 \times 10^{-6}\ A) \times \left(\frac{1}{18.5 \times 10^{-3}}\right) s$$

$$U_e = 9.5\ V \times \left(9.424 \times 10^{-6}\ A\right)\left(\frac{1}{18.5} \times 1000\right) s$$

$$U_e = 9.5\ V \times 9.424 \times 10^{-6})\ C/s \times (54.05\ s)$$

$$U_e = 4838.98 \times 10^{-6}\ V.C$$

$$U_e = 4.83898 \times 10^{-3} J \rightarrow \text{Eqn. 7}$$

Since the obtained value of U_e in Eqn. 7 is for a time of one second, and it can take as the output work done (W_e) per second. Therefore

$$W_e = 4.84 \times 10^{-3} Js^{-1} \rightarrow \text{Eqn. 8}$$

The Piezoelectric Nanogenerator device efficiency (PENG Efficiency) per second is, therefore, the output work efficiency (OWE) that can be calculated as the percentage ratio of W_e (From Eqn. 8) and W_d (From Eqn. 5)

$$OWE = \frac{W_e}{W_d}$$

$$\%OWE = \frac{W_e}{W_d} \times 100\ \%$$

$$\%OWE = \frac{4.84 \times 10^{-3}\,Js^{-1}}{3.70\ \times\ 10^{-2}Js^{-1}} \times 100\ \%$$

$$\%OWE = 13.1\ \%$$

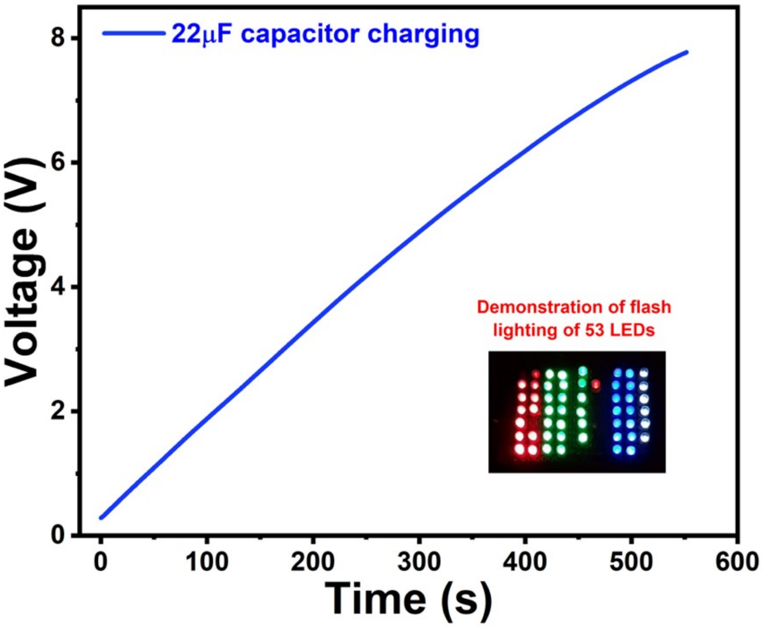

Figure S38. The voltage versus time graph shows the charging of a 22 μf capacitor.

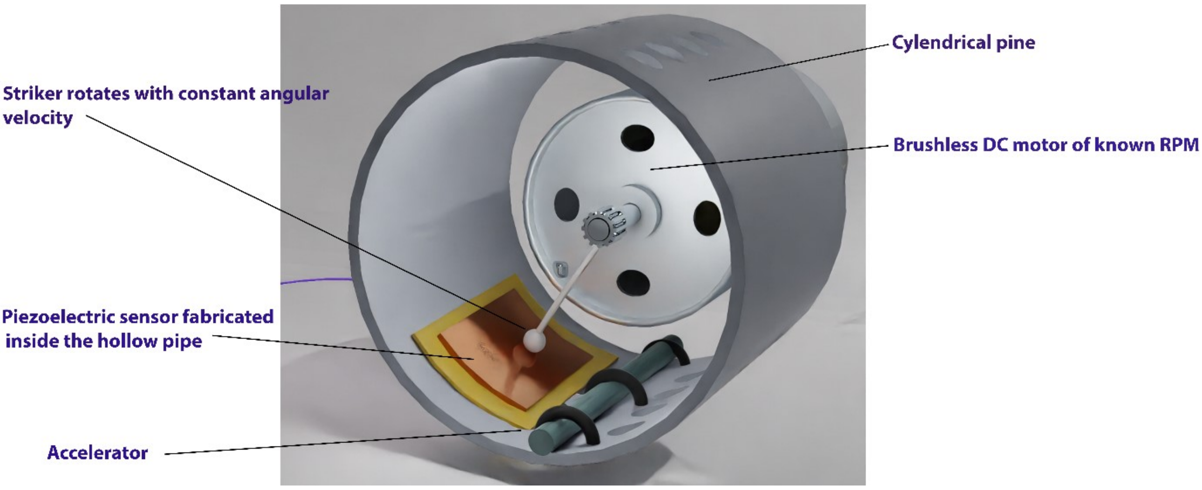

Figure S39. Geometrical design to measure the rotation per minute of a BLDC motor.

Supporting Discussion 3: Rotations per minute (RPM) calculation:

Let v be the speed of the BLDC motor, d be the inner circumference of the cylindrical pipe and r be the length of the striker from the shaft in time t (s)

$$speed\ (v) = \frac{distance\ (d)}{time\ (t)}$$

$$distance\ (d) = 2 * \pi * r$$

$$(v) = \frac{2 * \pi * r}{t}$$ m/s. → eqn. 1

If ω is the angular velocity of the striker shaft, then its frequency ϑ can be expressed as

$$frequency\ (\vartheta) = \frac{\omega}{2 * \pi}$$ → eqn. 2

The linear velocity v of the striker shaft can be expressed by $v = \omega * r$ → eqn. 3

Substituting eqn. 3 in eqn. 2, we get the frequency of the striker in revolutions per second (RPS).

$$(\vartheta RPS) = \frac{v}{2 * \pi * r}$$, multiplying this by 60 will give frequency in rotations per minute (RPM)

$$(\vartheta RPM) = \frac{v * 60}{2 * \pi * r} = \frac{30 * v}{\pi * r}$$ → eqn. 4

Substituting eqn. 1 in eqn. 4 we can calculate the RPM of the motor below

$$\vartheta RPM = \frac{30 * 2 * \pi * r}{\pi * r * t} = \frac{60}{t}$$ → eqn. 5

Hence, by knowing the time interval between the signals, the RPM of the motor can be calculated efficiently. In our measurements, the average ***t*** was found to be ~0.4 s, which gives rise to a uniform RPM value of 142.

Table S6. Comparison table of effective pressure, output V_{PP}. I_{PP} and output electrical energy of known organic composite energy harvesters.

Polymer composite compound devices	**Applied force, Frequency**	**Active area**	**Pressure**	**Output voltage**	**Current**	**Electrical energy in a second**	**Efficiency**	**Ref.**
$\{[Zn(PhPO(NH(C_6H_4COO))_2])(bpy)]\cdot(H_2O)_{1.5\,\infty}\}$/TPU	40 N	1.3 × 2 cm^2	0.154 MPa	5.6 V	16.094 µA	90.13 µJ	-	[8]
$[Ph_3MeP]_4[Ni(NCS)_6]$ / TPU	17 N	1.3 × 3 cm^2	0.044 MPa	19.29 V	14 µA	270.06 µJ	-	[9]
$[Ph_2(^iPrNH)_2P]\cdot PF_6$/PDMS	15 N	1.8 × 1 cm^2	0.083 MPa	8.5 V	0.5 µA	4.25 µJ	-	[10]
DPDP.PF_6/PDMS	15N,10 Hz	1.3 × 3 cm^2	0.038 MPa	8.5 V	0.5 µA	4.25 µJ	-	[11]
TPAP.BF_4/TPU	22 N, 8 Hz	1.3 × 3 cm^2	0.056 MPa	7.37 V	0.61 µA	4.49 µJ	-	[12]
TIAP.BF_4/TPU	22 N, 8 Hz	1.3 × 3 cm^2	0.056 MPa	4.75 V	0.41 µA	1.95 µJ	-	[13]

DPDP.BF_4/TPU	22 N, 8Hz	1.3×3 cm^2	0.056 MPa	8.95 V	0.89 μA	7.96 μJ	-	[14]
$FAPbBr_3$/PDMS	-----	1×3 cm^2	0.5MPa	8.5 V	11.4 μA	96.9 μJ	-	[13]
$MAPbBr_3$/PVDF	-----	2.4×1.5 cm^2	9.8 KPa	5V	0.06 μA	0.3 μJ	-	[14]
$MAPbI_3$/PVDF	7.5N, 4Hz	2.9×1.5 cm^2	0.017 MPa	220 mV	0.004 μA	0.00088 μJ	-	[15]
$[(PhCH_2NH)_6P_3N_3Me]I$, [PMe]I	21 N, 9 Hz	1.4×1.8 cm^2	0.0833 MPa	13.7 V	9.752 μA	133.6 μJ	-	[16]
DIPA·BNPP	**12 N, 8 Hz**	**2.5×2.5 cm^2**	**0.0192 MPa**	**9.5 V**	**7.7 μA**	**89.49 μJ**	**13.1 %**	**This work**

Table S7. Comparison table of effective pressure, power density, current density and voltage validation through capacitor charging in (%) of known organic composite energy harvesters.

Compound	**Voltage**	**Power density**	**Current density/current**	**Pressure**	**Highest stored voltage in capacitor**	**Charge stored**	**Ref.**
TMAB	10 V		4.46 μA				[17]
$MAPbBr_3$/PVDF	5 V	0.28 μW cm^{-2}	60 nA	9.8 kPa	3.64 mV		[14]
$MAPbI_3$/PDMS	108	0.3 mW m^{-2}	0.24 μA				[18]
$MAPbI_3$/PVDF	220 mV	0.8 mW m^{-2}	4 nA	17.2MPa	31.5 μV		[15]
$FASnI_3$/PVDF	23 V	35.05 mW cm^{-2}	6.15 μA cm^{-2}	0.1 MPa			[19]
$CsPbBr_3$/PVDF	10.3 V	3.31 μW	1.29 μA cm^{-2}	7.4 Pa	4 V		[20]
[BnNMe3]2CdBr4/PDMS	52.9 V	13.8 μW cm^{-2}	0.23 μA cm^{-2}	44.4 kPa			[21]
[BnNMe2nPr]2CdBr4/PDMS	63.8 V	37.1 μW cm^{-2}	0.59 μA cm^{-2}	44.4 kPa			[21]
DIPA·BNPP	**9.5 V**	**2.72 μW cm^{-2}**	**1.12 μAcm^{-2}**	**0.0192 MPa**	**22 μF, 8 V**		**This work**

DPDP·PF_6 = diphenyl diisopropylamino phosphonium hexaflurophosphate; TPU = thermoplastic polyurethane; DPDP·BF_4 = diphenyl diisopropylaminophosphonium tetrafluoroborate; TPAP·BF_4 = triphenyl isopropylaminophosphonium tetrafluoro borate; TIAP·BF_4 = tetraisopropylaminophosphonium tetrafluoro borate; Bn = benzyl; 4-BrBn = 4-bromobenzyl; 3NA = 3-nitroaniline; PCL = poly- -caprolactone; Boc-FF = Boc-Phe-Phe dipeptide; Boc = N-tert-butoxycarbonyl; Phe = L-Phenylalanine; PLLA = poly (L-lactic acid); PMMA = polymethylmethacrylate.

Table S8. Comparison table on various methods to calculate PENG energy efficiency.

S. No.	Systems Utilized/Methods	Method and efficiency	Advantages	Ref.
1	PVDF-nanofiber; direct method; Mechanical stretch and electrical poling; Efficiency	$ECE = \frac{Electrical\ energy\ Generated}{mechanical\ energy\ applied} = \kappa^2$ $ECE = 0.5\%\ to\ 2.6\%$	- Applicable for only piezoelectric polymer-based devices	22
2	Flextensional PZT structure/ direct method/Load shaker, vibration	$\eta = \frac{\frac{1}{2} \times C_{rec} \times V_{rec}^2}{\frac{1}{2} \times m \times v^2 \times t \times f}; \eta = 7.5\ \%$	- Applicable for the vibrational transducer - Applicable for shaker-type systems	23
3	Ceramics, Piezoelectric nanowires/ direct method	Electromechanical coupling $\chi = \frac{Electrical\ work\ performed\ by\ element}{Net\ energy\ supplied\ to\ element}$	- Based on the vibrational energy harvesting (VEH) cycle	24*
4	PZT/Stack-Membrane-Cantilever (Ball drop impact)/direct method	Electromechanical coupling $\eta = \frac{\frac{1}{2}[\frac{\kappa^2}{(1-\kappa^2)}]}{\frac{1}{Q} + \frac{1}{2}[\frac{\kappa^2}{(1-\kappa^2)}]} \times 100; \eta = 16.6\%$	- Energy efficiency is based on quantity factor and electromechanical coupling constant	25
5	**DIPA·BNPP**-PDMS/Indirect method	$\eta = \frac{Output\ electrical\ energy\ per\ unit\ time}{Input\ deformation\ energy\ per\ unit\ time}$ (as mention above) %OWE = 13.1%	- Utilizes the optimized applied frequency of the impact setup and from the nanogenerator output values for energy conversion efficiency calculation. - Applicable for all polymer composite devices - Both input and output work done is extracted from measurements and settings from the home-built impact setup	**This Work**

*Efficiency data for several ceramics can be obtained from this reference

References

1. J. Tauc, R. Grigorovici and A. Vancu, *Phys. Stat. Sol.*, 1966, **15**, 627-637.
2. P. Makuła, M. Pacia and W. Macyk, *J. Phys. Chem. Lett.*, 2018, **9**, 6814-6817.
3. G. Sheldrick, *Acta Cryst.* 2008, A **64**, 112–122.
4. M. Frisch*, et al.,* Gaussian 09, Revision C.01; Gaussian, Inc: Wallingford, CT 2016.
5. S. Kurtz and T. Perry, *J. Appl. Phys.*, 1968, **39**, 3798-3813.
6. F. Beer, E. Johnston, J. DeWolf and D. Mazurek, 2015.Mechanics of Materials (7th edition). McGraw-Hill.
7. C.-N. Xu, M. Akiyama, K. Nonaka and T. Watanabe, *IEEE transactions on ultrasonics, ferroelectrics frequency control*, 1998, **45**, 1065-1070.
8. N. Prajesh, V. B. Sharma, S. S. Rajput, C. K. Singh, P. Dixit, B. Praveenkumar, J. K. Zaręba, D. Kabra, S. Ogale and R. Boomishankar, *ACS Sustain. Chem. Eng.*, 2022, **10**, 9911-9920.
9. T. Vijayakanth, F. Ram, B. Praveenkumar, K. Shanmuganathan and R. Boomishankar, *Angew. Chem. Int. Ed.*, 2020, **59**, 10368-10373.
10. A. Graja, *Phys. Stat. Sol.*, 1968, **27**, K93-K97.
11. T. Vijayakanth, A. K. Srivastava, F. Ram, P. Kulkarni, K. Shanmuganathan, B. Praveenkumar and R. Boomishankar, *Angew. Chem. Int. Ed.*, 2018, **130**, 9192-9196.
12. T. Vijayakanth, F. Ram, B. Praveenkumar, K. Shanmuganathan and R. Boomishankar, *Chem. Mater.*, 2019, **31**, 5964-5972.

13. R. Ding, H. Liu, X. Zhang, J. Xiao, R. Kishor, H. Sun, B. Zhu, G. Chen, F. Gao and X. Feng, *Adv. Funct. Mater.*, 2016, **26**, 7708-7716.
14. A. Sultana, M. M. Alam, P. Sadhukhan, U. K. Ghorai, S. Das, T. R. Middya and D. Mandal, *Nano Energy*, 2018, **49**, 380-392.
15. A. Sultana, S. K. Ghosh, M. M. Alam, P. Sadhukhan, K. Roy, M. Xie, C. R. Bowen, S. Sarkar, S. Das and T. R. Middya, *ACS Appl. Mater. Interfaces*, 2019, **11**, 27279-27287.
16. S. Deswal, R. Panday, D. R. Naphade, P. A. Cazade, S. Guerin, J. K. Zaręba, A. Steiner, S. Ogale, T. D. Anthopoulos and R. Boomishankar, *Small*, 2023, **19**, 2300792.
17. Y. Zhang, M. A. Hopkins, D. J. Liptrot, H. Khanbareh, P. Groen, X. Zhou, D. Zhang, Y. Bao, K. Zhou and C. R. Bowen, *Angew. Chem. Int. Ed.*, 2020, **59**, 7808-7812.
18. J. Dhar, S. Sil, N. A. Hoque, A. Dey, S. Das, P. P. Ray and D. Sanyal, *ChemistrySelect*, 2018, **3**, 5304-5312.
19. S. Kahmann, O. Nazarenko, S. Shao, O. Hordiichuk, M. l. Kepenekian, J. Even, M. V. Kovalenko, G. R. Blake and M. A. Loi, *ACS energy Lett.*, 2020, **5**, 2512-2519.
20. Y. Li, M.-h. Xu, Y.-s. Xia, J.-m. Wu, X.-k. Sun, S. Wang, G.-h. Hu and C.-x. Xiong, *Chemical Engineering Journal*, 2020, **388**, 124205.
21. S. Deswal, S. K. Singh, P. Rambabu, P. Kulkarni, G. Vaitheeswaran, B. Praveenkumar, S. Ogale and R. Boomishankar, *Chem. Mater.*, 2019, **31**, 4545-4552.
22. C. Chang, V. H. Tran, J. Wang, Y.-K. Fuh and L. Lin, *Nano Lett.*, 2010, **10**, 726-731.
23. H. W. Kim, A. Batra, S. Priya, K. Uchino, D. Markley, R. E. Newnham and H. F. Hofmann, *Jpn J. Appl. Phys.*, 2004, **43**, 6178.
24. S. Crossley and S. Kar-Narayan, *Nanotechnology*, 2015, **26**, 344001.
25. J. Cho, R. Richards, D. Bahr, C. Richards and M. Anderson, *Appl. Phys. lett.*, 2006, **89**.